Cdh-2 modulates cortical F-actin distribution to establish stiffness gradients driving forebrain roof plate invagination

Meenu Sachdeva,[1,2] Prasenjit Sharma,[3] Pankaj Gupta,[1,2] Mohd Ali Abbas Zaidi [1,4] Sweta Kushwaha,[1,2] Jonaki Sen[1,2,] * †

1. Department of Biological Sciences and Bioengineering, Indian Institute of Technology Kanpur, Kanpur, 208016, Uttar Pradesh, India
2. Mehta Family Center for Engineering in Medicine (MFCEM), Indian Institute of Technology Kanpur, Kanpur, 208016, Uttar Pradesh, India
3. Department of Mechanical Engineering, Indian Institute of Technology Kanpur, Kanpur, 208016, Uttar Pradesh, India
4. Department of Biochemistry and Molecular Biology, University of Nebraska Medical Center, Omaha, NE, 68198, USA.

† Lead Contact: jonaki@iitk.ac.in

Graphical Abstract

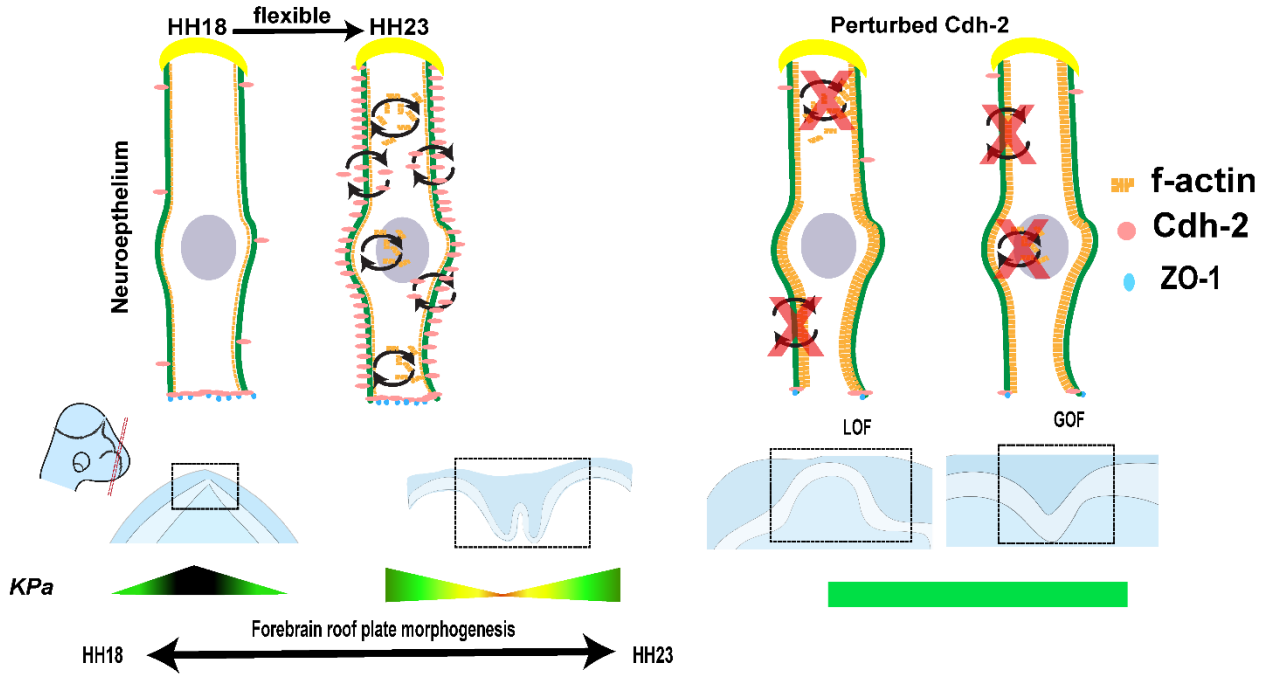

Abstract

The invagination of the embryonic forebrain roof plate is critical for cerebral hemisphere formation. Disruption of this process leads to holoprosencephaly (HPE), a severe congenital brain malformation.

Although mutations in several genes have been linked to HPE and studies using the chick embryo have implicated certain signaling pathways, yet the mechanisms by which mechanical signals are translated into tissue morphological changes remain poorly understood. To address this lacuna, we employed atomic force microscopy to map spatiotemporal stiffness gradients across the dorsal forebrain in the chick embryo during roof plate invagination. Our analysis revealed that the initial uniformly elevated levels of stiffness across the roof plate are dramatically altered during morphogenesis. A pronounced stiffness gradient emerges, whereby the roof plate midline becomes markedly more compliant than dorsolateral regions. Through expression screening, we identified Cdh-2 as a candidate mechanical regulator whose spatiotemporal expression pattern precisely mirrors the observed stiffness gradient. Both loss- and gain-of-function perturbations of Cdh-2 disrupted the normal stiffness gradient and caused significant architectural alterations, such as evagination or a V-shaped invagination of the roof plate. Mechanistically, Cdh-2 modulates tissue stiffness by regulating adherens junction stability and cortical F-actin distribution along the apicobasal axis of neuroepithelial cells. These findings provide critical insights into the mechanical forces and molecular interactions governing forebrain roof plate morphogenesis, highlighting the importance of Cdh-2, and shedding light on the pathogenesis of HPE.

Teaser

Cdh-2 and cortical actin distribution interact to establish stiffness gradients directing forebrain roof plate invagination.

Introduction

During embryonic development, the coordinated integration of signaling pathways and physical forces ensures the precise formation of complex three-dimensional structures (*1, 2*). Morphogenesis of the vertebrate forebrain serves as a prime example, whereby the hollow vesicle-like forebrain is partitioned into two chambers that form the cerebral hemispheres. Failure of this process results in holoprosencephaly (HPE), one of the most common and severe congenital brain malformations in humans (*3, 4*). The dorsal forebrain consists of a pseudostratified neuroepithelium overlaid by a layer of mesenchyme that later contributes to the meninges. In the developing chick embryo, this bilayer structure undergoes a precisely orchestrated series of morphological changes, beginning with the formation of a characteristic "pucker" in

the dorsal midline at stage HH (Hamburger & Hamilton)19(*5*), which subsequently develops into a distinctive W-shaped invagination by HH23. Previously, we showed that the interplay of canonical and non-canonical BMP signaling pathways establishes differential thickness of the roof plate neuroepithelium, which is critical for its invagination (*6*). In addition, we showed that retinoic acid signaling contributes to the spatial patterning and morphogenesis of the roof plate (*7*). Nonetheless, the mechanisms through which these signaling pathways and other factors regulate invagination of the forebrain roof plate remain to be elucidated.

Recent advances in mechanobiology have revealed that physical forces and molecular signals play equally important roles in shaping embryonic tissues (*8*). The mechanical properties of developing brain tissue, particularly tissue stiffness, have emerged as key regulators of morphogenetic processes. In fact, it was demonstrated using atomic force microscopy (AFM) that tissue stiffness varies spatially and temporally during development of the mouse cortex, creating gradients that guide cellular behaviors and tissue architecture (*9*). On the other hand, the differential adhesion hypothesis (DAH) provides a foundational framework for understanding how differences in the strength of adhesion between cells drive tissue morphogenesis. According to this hypothesis, tissues behave like immiscible liquids, with surface and interfacial tensions arising from the differential adhesion energies between motile cells (*10*). However, recent findings suggest that the relationship between adhesion and tissue mechanics is more complex than originally envisioned because it involves dynamic interactions between adhesion molecules, cytoskeletal networks, and mechanical forces (*11*). It must be noted that in the context of the forebrain roof plate, whether differential tissue stiffness and/or adhesion plays a role in its invagination remains unexplored.

Classical cadherins are critical mediators of cell-cell adhesion and mechanotransduction during development (*12*). These calcium-dependent adhesion molecules function closely with the actin cytoskeleton through multiple mechanisms. Cadherin complexes bind actin filaments through mechanosensitive proteins such as α-catenin, vinculin, and EPLIN (*13*). Independently, cadherins regulate actin dynamics and filament organization at cell-cell junctions by recruiting proteins that control actin polymerization and crosslinking (*14*). The association of cadherins with the actin cytoskeleton allows cadherin junctions to couple with actomyosin contractile networks, enabling force transmission across tissues. The contractile force generated

by the actin cytoskeleton underneath the plasma membrane is referred to as the cortical tension, which minimizes the cell surface area and maintains the cell shape. This tension is primarily generated and regulated by actomyosin contractility, and is transmitted across the cell cortex, influencing the mechanical properties of both individual cells and tissues. At cell-cell contacts, adhesion tension arises from the active recruitment of cadherin at cell junctions, which reduces the interfacial tension at the contact site by promoting strong homophilic binding between adjacent cells (*15*). Adhesion tension thus acts as a counterforce to cortical tension, facilitating the expansion of cell-cell contact zones and stabilizing tissue architecture. The balance between these two forces, cortical tension pulling to minimize the contact area and adhesion tension expanding it, determines the size and stability of cell-cell junctions (*16*). The resulting patterns of cortical tension create spatial heterogeneities that drive morphogenetic processes, including cell rearrangement, tissue folding, and boundary formation.

Large morphological changes were observed during the invagination of the forebrain roof plate. Despite advances in understanding the molecular aspects of forebrain morphogenesis (*6, 7, 17*), several fundamental questions remain unanswered. For example, it is not known how mechanical forces and molecular signals are integrated to control the precise timing and location of morphogenetic events. Although accumulating evidence demonstrates that tissue stiffness functions as both a consequence and driver of morphogenetic processes, whether cell adhesion molecules play a key role in regulating roof plate morphogenesis and how they translate molecular interactions to tissue-level mechanical properties remains to be elucidated. In this study, using the developing chick forebrain as a model, we addressed these pertinent questions using atomic force microscopy combined with molecular perturbation-based approaches. We discovered that the classical cadherin molecule, N-cadherin/Cdh-2 (Cdh-2), plays a critical role in regulating tissue stiffness and morphogenesis in the forebrain roof plate through alterations in adherens junction stability and distribution of F-actin along the cell cortex.

Results

Spatiotemporal changes in stiffness of the forebrain roof plate and overlying mesenchyme during morphogenesis

Visible morphological changes in the dorsal forebrain of the chick begins at embryonic day 3 (stage HH18). To observe these changes more closely, we harvested chick embryos at various stages and prepared coronal sections spanning the mid-anterior to mid-posterior regions of the forebrain (Figure 1A). These sections were stained with DAPI to label the nuclei, and we observed that the forebrain was elliptical in shape at HH18 (Fig. 1B and B'). However, at HH19, a "pucker" appeared in the middle of the neuroepithelium (NE) in the dorsal region known as the roof plate (Fig. 1C and C') and the roof plate midline began to invaginate (move inwards) in the form of a shallow "W" by HH21 (Fig. 1D and D'). This invagination deepened further and at HH23 it was in the shape of a completely formed "W" (Fig. 1E and E'). In contrast, the morphology of the overlying mesenchyme remained relatively unchanged throughout this period, although there was a consistent increase in thickness from HH19 to HH23, particularly in regions just above the troughs of the W-shaped roof plate invagination, which we refer to as midline vortices (yellow asterisk in Fig. 1E').

The dramatic morphological changes in the dorsal forebrain during invagination led us to hypothesize that these changes could be linked to concurrent changes in tissue stiffness. To establish if this is true, we proposed to independently quantify the stiffness of the dorsal forebrain neuroepithelium and the overlying mesenchyme between the developmental time windows of HH18 and HH23. In the absence of an established protocol for preparing chick (Gallus gallus) samples for atomic force microscopy (AFM), we first optimized the protocol for conducting contact-mode AFM on the embryonic chick forebrain (Fig. S1). The dorsal forebrain midline spans a substantial length of up to 1000 µm, while the contact area of the AFM probe covers only approximately 10 nm; hence, we divided the neuroepithelium and the overlying mesenchyme into distinct zones for systematic measurement (Fig. S1, S2, and S3). At HH18, the midline apex (MA) (Fig. 1F) of the neuroepithelium exhibited stiffness averaging at 818 kPa (Fig. 1J), while in the dorsolateral regions (DL), it was 361 kPa. On the other hand, the mesenchyme stiffness averaging at ~ 576 kPa at the

midline (MMA), although lower than that of the neuroepithelium MA, is much elevated compared to the stiffness of the dorsolateral mesenchyme (MDL) averaging at 223.5kPa (Fig. 1L).

At HH19 (~6 Hrs. later), the roof plate domain expands, and the "pucker" appears in the middle of the neuroepithelium (Fig. 1C' and G). The midline apex (MA) of the neuroepithelium at HH19 exhibited a stiffness of ~ 141 kPa, which was significantly lower than that of the MA region at HH18, whereas in the dorsolateral (DL) region, the stiffness remained nearly the same as that of HH18 (Fig. 1J). At this stage, the stiffness of the mesenchyme above the midline apex (MMA) decreased to 395 kPa; however, in the regions adjacent to the midline vortex (MMV), it was significantly elevated to nearly 690 kPa (Fig. 1L). Thus, the stiffness of the neuroepithelium exhibits a sharply decreasing trend, making it more flexible, while the stiffness of the overlying mesenchyme rises at sites where the neuroepithelium will undergo bending in future (Fig. 1G, J, and L). At HH21, the stiffness of the neuroepithelium at the midline apex (MA) further declined to 67 kPa, whereas at the dorsolateral (DL) regions, it remained largely unchanged, thus exhibiting a pronounced gradient of stiffness across the W-shaped region (Fig. 1J). In the mesenchyme, the areas directly above the midline vortices (MMV), where bends in the neuroepithelium are observed, exhibit significantly elevated levels of stiffness (~780 kPa). In contrast, the stiffness of the mesenchyme in other regions, such as just above the midline apex (MMA) and above the dorsolateral neuroepithelium (MDL), remained at significantly lower levels (Fig. 1L). This gradient of stiffness across the invaginating neuroepithelium was quite apparent at HH23 (Fig. 1K), while the stiffness of the mesenchyme above the midline vortex (MMV) remained significantly elevated at ~700 kPa at this stage (Fig. 1M).

The discovery of variations in tissue stiffness across the dorsal forebrain at different stages of development highlights the spatiotemporal dynamics of the mechanical properties of the neuroepithelium and overlying mesenchyme. We observed that with progress in development, the stiffness of the neuroepithelium, which was high in the midline and relatively low in the dorsolateral regions at HH18, exhibited an inverse gradient across the roof plate at HH23, such that the midline became considerably less stiff compared to the dorsolateral regions. The mesenchyme on the other hand, maintains moderate levels of stiffness above the dorsal neuroepithelium, except for the regions above the midline vortices (MMV) which become extremely stiff as the invagination of the neuroepithelium progresses. Thus, it is likely that the localized increase in

stiffness of the mesenchyme provides the necessary force to drive invagination of the relatively more flexible neuroepithelium underneath.

Cdh-2 exhibits a spatiotemporal expression pattern that aligns with changes in roof plate stiffness during morphogenesis.

Spatiotemporal profiling of stiffness in the dorsal forebrain led us to speculate that midline invagination might be significantly influenced by mechanical forces that operate in real time alongside biochemical pathways (*9*). In general, sites where cells adhere to each other serve as force-sensing hubs (*18*). These sites are enriched in cadherins, which facilitate physical connections between neighboring cells through both trans- and cis-extracellular interactions and cytoplasmic associations with the actin cytoskeleton (*19*). To decipher the molecular basis of differential stiffness in the dorsal forebrain, we performed an expression screen using RNA *in situ* hybridization to identify candidate cell adhesion molecules involved in this process. We identified N-Cadherin/Cadherin-2 (Cdh-2) as a strong candidate, as it exhibited relatively high levels of expression in the W-shaped invaginating region of the roof plate compared to the dorsolateral regions of the neuroepithelium (Fig. 2A and A'). In the chick embryo, the walls of the forebrain anlagen are of variable thickness, comprising a single layer of neuroepithelial cells, with each cell spanning the apical-basal axis. The nuclei of neuroepithelial cells are positioned at different levels, giving it a multilayered appearance; hence, it is referred to as pseudostratified neuroepithelium. The apical side, adjacent to the lumen, contains apical adherens junctions, while the basal side lies adjacent to the mesenchyme (Fig. 2B, B' and B''). We carried out immunohistochemistry on sections of the chick forebrain from stages spanning HH10 to HH23 to determine the expression of Cdh-2 and we found that between HH14 to HH18, Cdh-2 is specifically localized to the apical side of the neuroepithelium (Fig. 2C, D and E). From HH18 onwards, we observed that, in addition to the apical side, Cdh-2 protein could also be detected on the lateral and basal sides of the neuroepithelial cells present in the middle region of the roof plate (Fig. 2E, E, ' F, F, ' G, H, and H'). The distribution of Cdh-2 protein is shown schematically in Fig. 2J. The intensity of immunostaining progressively increased from HH18 to HH23 (Fig. 2I), indicating an increase in protein expression. It must be noted that although Cdh-2 exhibits differential expression across the roof plate neuroepithelium, we could not detect any expression of Cdh-2 in the mesenchyme. Interestingly, a strong correlation (R^2 =0.76) was

observed when comparing the spatiotemporal changes in stiffness with the presence of the Cdh-2 protein in the midline apex region of the neuroepithelium (Fig. 2K). In fact, the prominent appearance of Cdh-2 protein at HH19 in the basal and lateral regions of cells in the neuroepithelium coincided with the dramatic decrease in stiffness of the neuroepithelium in this region (Fig. 2I, K, and L). These intriguing observations motivated us to further investigate the possible role of Cdh-2 in determining the stiffness of the roof plate and regulating its invagination.

Cdh-2 regulates invagination as well as patterning of the forebrain roof plate

We utilized loss-of-function (LOF) and gain-of-function (GOF) strategies to manipulate the function of Cdh-2 and gain insight into its possible role in the morphogenesis of the forebrain roof plate. For LOF, we generated a construct that expresses a dominant-negative version of Cdh-2 lacking the extracellular binding domain (DN-Cdh-2) (*20*) and cloned it into the pCAG-IRES-GFP vector (Fig. S4). When expressed in excess, DN-Cdh-2 interferes with the interactions between the extracellular domains of adjacent cis- or trans-configured Cdh-2 molecules (*21*). In addition, we generated a construct for RNA interference-mediated knockdown of Cdh-2 (Cdh-2 RNAi) and cloned it into the pRmiR vector (*22*) (Fig. S4). The knockdown efficacy of Cdh-2 RNAi was determined using a sensor assay (Fig. S5). Upon electroporation of either DN-Cdh2 or Cdh-2 RNAi to create the LOF of Cdh-2 (Fig. 3A), we observed a dramatic morphological change in the roof plate, whereby it evaginated (protruded outwards) instead of undergoing invagination (bending inward) (compare Fig. 3B with 3C and Fig. 3D with 3E, respectively). This evagination phenotype was more pronounced in the case of the LOF generated through RNAi-mediated knockdown of Cdh-2 (Fig. 3C) than in the LOF generated through expression of DN-Cdh-2 (Fig. 3E). For gain-of-function (GOF), we co-electroporated a construct with full-length Cdh-2 (Cdh-2 FL) (Fig. S4) and a construct expressing GFP (pCAG-GFP) to mark electroporated cells in the chick forebrain. Electroporation was conducted at HH10 and the tissue was harvested at HH23 (Fig. 3A). We observed that the morphology of the forebrain roof plate was significantly altered, and the invagination was V-shaped, as opposed to the W-shaped invagination in the control (Fig. 3F and G).

In a previous study carried out by our group, we observed dramatic changes in forebrain roof plate invagination upon manipulation of the RA signaling. These morphological changes are accompanied by

alterations in the patterning of the roof plate, as gauged by differences in the expression patterns of certain roof plate marker genes (*7*). Thus, we were curious to determine whether the LOF and/or GOF of Cdh-2 would affect patterning of the forebrain roof plate. We examined the expression of various markers such as WNT7B, BMP7, and CYP26A1 and found that the expression of WNT7B was completely lost with the GOF of Cdh-2 (Fig. 3H, H', J, and J'), whereas with LOF it was present in the lateral regions of the evaginated roof plate (Fig. 3H, H, ' I, and I'). BMP7, which is expressed only in the middle loop of the W-shaped invagination in the control, was completely absent in both the LOF and GOF of Cdh-2 (Fig. 3K, K', L, L', M, and M'). Further, with both LOF and GOF of Cdh-2 we observed a dramatic reduction in the expression of CYP26A1, which became restricted to very few cells (Fig. 3N, N', O, O', P, and P'). Overall, we observed a significant alteration in the marker expression and patterning of the dorsal forebrain upon functional perturbation of the Cdh-2.

Cdh-2 mediates spatiotemporal variability in stiffness of the roof plate during its invagination.

We observed that spatiotemporal changes in the stiffness of the dorsal forebrain tissues were closely correlated with the expression of Cdh-2 in the neuroepithelium. Further, upon perturbation of Cdh-2, dramatic morphological changes were observed. Together, these findings prompted us to investigate the effect of functional manipulation of Cdh-2 on tissue stiffness. Stiffness was measured using AFM after electroporation with Cdh-2 loss-of-function (LOF) and gain-of-function (GOF) constructs at HH23 (Fig. S6) when the W-shaped invagination was prominent in the dorsal forebrain of the chick embryo (Fig. 4A and A'). In the LOF condition at HH23, the stiffness was uniformly elevated across the evaginated roof plate neuroepithelium, averaging approximately 308 kPa at the midline apex and 358 kPa in the midline lateral regions. These values approached levels comparable to those of the dorsolateral neuroepithelium of the control roof plate at the same stage, which measured 389 kPa (Fig. 4B, B', D, F, G, and H). This suggests that the LOF of Cdh-2 abolishes the stiffness gradient normally present from the midline to the dorsolateral regions of the neuroepithelium and increases stiffness uniformly across the dorsal forebrain (Fig. 4F, G, and H). Contrary to our expectations, the GOF of Cdh-2 also led to increased stiffness at the midline relative to the control, although it remained lower than that of the dorsolateral mesenchyme (Fig. 4C, C', D, F, G, and

H). The stiffness of the dorsolateral neuroepithelium, however, was comparable to that of the control in both LOF and GOF conditions (Fig. 4D, F, G, and H).

Interestingly, when assessing the stiffness of the mesenchyme following LOF and GOF of Cdh-2 cells, we observed a significant decline in stiffness compared to the control. It is important to note that, while Cdh-2 is expressed in the roof plate neuroepithelium, it is undetectable in the mesenchyme. Normally, at HH23, mesenchymal stiffness is relatively uniform, except in the region above the midline vortices, where it is significantly high at approximately 700 kPa (Fig. 4E, F, G, and H). However, with the LOF of Cdh-2 in the neuroepithelium, the mesenchymal stiffness above the vortices decreased to approximately 305 kPa, which is close to that of the dorsolateral mesenchyme, resulting in overall reduced mesenchymal stiffness. On the other hand, with GOF of Cdh-2, stiffness of the mesenchyme in the vortex region overlying the midline was also dramatically reduced to approximately 94.3 kPa, possibly leading to the mesenchyme exerting much less force on the underlying neuroepithelium (Fig. 4E, F, and H). This raises the following question: Under the GOF condition, how was the neuroepithelium undergoing bending to give rise to the V-shaped invagination if the overlying mesenchyme was much less stiff and, hence, could not apply the necessary force?

Our earlier observations suggest that invagination of the forebrain roof plate is initiated by the formation of the “pucker” at HH19. Subsequently, the neuroepithelium on either side of this “pucker” bends inward to give rise to the W-shaped morphology of the invagination at HH23. Therefore, we speculated that the morphological consequences of the LOF and GOF of Cdh-2 observed at HH23 could result from the disruption of Cdh-2 function at HH19. To explore this, we examined the morphological changes in HH19 following Cdh-2 perturbation. We observed that upon LOF, the neuroepithelium was flattened with no discernible pucker (Fig. 4I and J), whereas GOF produced a subtle dip at HH19 that likely developed into a V-shaped invagination at later stages (Fig. 4I and K). We were intrigued by the fact that LOF leads to evagination at HH23, despite both the mesenchyme and neuroepithelium having uniform stiffness. In contrast, GOF leads to bending of the neuroepithelium, resulting in a V-shaped invagination at HH23, despite the mesenchyme above the midline neuroepithelium being much less stiff.

To investigate this further, we measured the stiffness of the neuroepithelium and mesenchyme at HH19, following the LOF and GOF of Cdh2 (Fig. S7). We found that, following LOF at HH19, stiffness across the dorsal neuroepithelium was uniform (~216 kPa), unlike in the control, where the stiffness was graded with the midline apex being much less stiff (~ 41 kPa) than the midline lateral region (~ 211 kPa) (Fig. 4L, N, O, and P). Similarly, with the GOF of Cdh-2, the stiffness of the dorsal neuroepithelium was close to 96 kPa, which is lower than the stiffness at both the midline apex and midline lateral regions in the control (Fig. 4L, N, O, and P). This indicated that with GOF, there was a decrease in stiffness, as well as an abolition of the gradient of stiffness across the neuroepithelium. Moreover, consistent with observations at HH23, disruption of Cdh-2 significantly modified the stiffness of the overlying mesenchyme at HH19, with an overall stiffness reduction observed in both LOF and GOF compared to the control. With LOF, the stiffness of the neuroepithelium was ~216 kPa, and that of the mesenchyme was ~189 kPa (Fig. 4L, M, N, and O). Thus, the mesenchyme was less stiff than the neuroepithelium at HH19, which could explain why it underwent evagination (Fig. 4P). Conversely, GOF resulted in a higher mesenchymal stiffness (~208 kPa), providing the necessary force for neuroepithelial bending. Simultaneously, it lowered the stiffness of the midline neuroepithelial region to ~92 kPa, making it less stiff than the dorsolateral region, thus leading to a V-shaped invagination (Fig. 4P). The distinct morphological defects in the roof plate, that is, evagination with the LOF and V-shaped invagination with the GOF, likely arise from a failure to establish the crucial stiffness gradient necessary for pucker formation at HH19. Thus, these morphological abnormalities appear to result from disrupted or misdirected mechanical cues caused by functional perturbation of Cdh-2. Although distinctive morphological phenotypes were observed under Cdh-2 LOF and GOF conditions, the overall changes in tissue stiffness were remarkably similar. Both the LOF and GOF abolished the stiffness gradient extending from the midline of the roof plate neuroepithelium, resulting in a more or less uniform stiffness profile. To investigate the mechanism by which LOF and GOF may lead to similar changes in tissue stiffness, we performed immunohistochemistry for Cdh-2 in the control and GOF forebrain sections at HH23. Contrary to expectations that GOF would increase Cdh-2 expression, we observed a significant decrease in Cdh-2 immunostaining in electroporated regions with GOF compared to the control (Fig. S8). A similar pattern was observed at HH19 in forebrain sections electroporated with GOF constructs. Based on these observations, we hypothesize that a feedback mechanism is activated in response to Cdh-2 overexpression,

leading to the downregulation of endogenous Cdh-2. This reduction in Cdh-2 expression likely accounts for the similar neuroepithelial stiffness changes observed under both the LOF and GOF conditions.

Cdh2 translates mechanical cues through adherens junctions and not through direct regulation of cell proliferation.

Certain tissue contexts have a high cell density and greater connectivity, such that cells are more tightly packed and interconnected, which restricts their movement. This collective behavior leads to a solid-like state, in which the tissue has increased mechanical rigidity and resists deformation. On the other hand, a lower cell density or reduced connectivity results in a more fluid-like state, where the tissue flows and cells have greater motility (*23*). Cell density can be regulated by factors such as cell proliferation and death; hence, differential proliferation rates within a tissue may induce tissue buckling, leading to invagination of the forebrain roof plate midline (*7, 17*). At HH23, the chick forebrain neuroepithelium was highly proliferative throughout, except for the dorsal forebrain midline, corresponding to the middle loop of the W-shaped invagination. This indicates that differential proliferation is a distinctive feature of the neuroepithelium of the dorsal forebrain. To determine whether Cdh-2 plays a role in the establishment of differential cell proliferation in this context, we perturbed its function and assessed its effect on cell proliferation by immunohistochemical detection of phospho-histone 3 (PH3), which marks the mitotic phase of the cell cycle (Fig. S9A, D, B, E, C, F). Quantification of PH3-positive cells in both the midline and dorsolateral neuroepithelium following LOF of Cdh-2 revealed a significant increase in proliferation at the midline compared with the control. However, gain-of-function (GOF) perturbation did not produce a significant change in the number of proliferating cells in either the midline or dorsolateral regions (Fig. S9G). As Cdh-2 perturbation also alters neuroepithelial morphology in the dorsal forebrain, we investigated whether these morphological defects were a secondary consequence of changes in proliferation. Therefore, we perturbed Cdh-2 in the lateral neuroepithelium, followed by the assessment of cell proliferation through immunohistochemical detection of PH3 (Fig. S9H, I, J, H). Quantification of GFP and PH3 double-positive cells during LOF and GOF in the lateral neuroepithelium revealed no change in proliferation (Fig. S9L) or morphology at this location. Thus, the observed effect on cell proliferation in the roof plate likely resulted

from context-dependent morphological and patterning changes caused by functional perturbation of Cdh-2 in the roof plate.

To understand how Cdh-2 links molecular interactions to tissue-level mechanical properties, we examined adherens junctions, where high levels of Cdh-2 are observed. ZO-1 localizes to cadherin-based contacts through direct interaction with the cadherin–catenin complex (Fig. 5A) (*24*). It scaffolds cadherin adhesion to the actin cytoskeleton and modulates mechanical forces at apical adherens junctions (*25*). In the absence of ZO-1, cadherin-containing junctions form but fail to properly connect to the cytoskeleton, weakening mechanical forces and stability (*26*). We observed that ZO-1 immunostaining was closely localized with Cdh-2 throughout the apical side of the forebrain neuroepithelium (Fig. 5B, B', C, C,' D, and D'). This led us to examine the effect of Cdh-2 perturbation on ZO-1 at the apical adherens juctions. In both LOF and GOF for Cdh-2, immunohistochemical detection of ZO-1 expression revealed decreased levels within the electroporated regions compared to the control (Fig. 5E, E', G, and G'), with a more pronounced reduction in ZO-1 observed with GOF for Cdh-2 (Fig. 5E, E', F, and F'). Thus, adherens junctions appear to be disrupted by either the LOF or the GOF of Cdh-2. ZO-1 is essential for maintaining Cdh-2 at apical adherens junctions and for preserving tissue shape. This is selectively impaired by the depletion of ZO-1, leading to destabilized mechanical properties consistent with the stiffness changes observed with both the LOF and GOF of Cdh-2. Taken together, these results indicate that Cdh-2 controls cell-cell adhesion dynamics and mechanical stability at apical junctions through ZO-1, which is essential for proper forebrain roof plate invagination.

Dynamic F-actin accumulation in the cortex of neuroepithelial cells mediated by Cdh-2 underlies spatiotemporal variability in roof plate stiffness

We observed that functional perturbation of Cdh-2 either through LOF or GOF resulted in ZO-1 depletion. However, ZO-1 is only present in apical adherens junctions; hence, the effects of its depletion should only be limited to the apical side. However, perturbation of Cdh-2 alters the stiffness of the entire tissue; hence, this raises the question of how mechanical cues are transmitted across the entire length of the cell along the apicobasal axis. ZO-1 and Cdh-2 cooperate to establish and maintain apical adherens junctions by physically

linking the cadherin–catenin complex to the tight junction scaffold and underlying actin cytoskeleton. Yu et al. proposed a mechanistic model wherein a positive feedback loop at cell-cell junctions involving cadherin causes trans-dimerization-induced local actin polymerization and actin tethering-induced cadherin immobilization and accumulation (*27*). This process directs the formation of a uniform actin mesh beneath the cell membrane (cell cortex).

Inspired by this model, we examined the distribution of F-actin in phalloidin stained neuroepithelial cells following Cdh-2 perturbation. We quantified the intensity of phalloidin staining up to 80 µm distance into the cell, both from the apical and basal sides of the neuroepithelium in sections of the forebrain roof plate (Fig. S9). Since phalloidin binds to F-actin, the intensity of phalloidin staining can serve as a measure of the amount of F-actin. Upon perturbation of Cdh-2, the following aberrant changes in F-actin levels were evident at HH23: LOF of Cdh-2 led to a significant increase in accumulation of F-actin on the apical side, whereas GOF led to a symmetric increase in F-actin across the entire apicobasal axis in the midline apex and vortex regions, with no change in F-actin distribution and levels in the dorsolateral neuroepithelial cells (Fig. 6G, H, and I). The increased accumulation of apical F-actin at HH23 correlated with the increase in stiffness observed in the LOF of Cdh-2.

We also measured F-actin accumulation in the neuroepithelial cells at HH19, the stage at which the "pucker" formation was observed in the roof plate midline. In the control, in the midline apex region where the "pucker" is present, F-actin accumulation was significantly high in the apical as well as the basal sides of the neuroepithelium, while it was uniformly low across the apico-basal axis in the dorsolateral regions. However, both LOF and GOF of Cdh-2 led to significant changes in F-actin accumulation along the apicobasal axis compared with the control, particularly in the midline region (Fig. 6J and K). Specifically, the LOF of Cdh-2 reduced F-actin accumulation significantly on the apical side of the midline neuroepithelium, while GOF led to a symmetric decrease in F-actin accumulation across the apicobasal axis in the midline regions (Fig. 6L). These observations demonstrate that Cdh-2 perturbation disrupts the cortical F-actin distribution along the apicobasal axis of neuroepithelial cells.

The concentration of Cdh-2 at the cell membrane of neuroepithelial cells determines the adhesivity between them and generates adhesive force (adhesion tension) throughout the tissue. In contrast, cortical F-actin

accumulation influences cellular morphology, such that increased F-actin levels reduce cellular flexibility and generate a counteracting force, that is, cortical tension. The balance between Cdh-2-mediated adhesion and F-actin-generated cortical tension determines precise cellular organization within a tissue. In this regulatory framework, the modulation of Cdh-2 expression directly influences the pattern of F-actin accumulation. Furthermore, Cdh-2 expression directly modulates the stiffness of the dorsal forebrain. We hypothesized that the precise spatiotemporal accumulation of Cdh-2 at the cell surface and F-actin in the cortex determines neuroepithelial stiffness. The establishment of a normal stiffness gradient is critical for the formation of a pucker at HH19. Upon Cdh-2 loss-of-function (LOF), increased tissue stiffness resulting from biased cortical F-actin accumulation prevents the roof plate from achieving sufficient flexibility to form the characteristic W-shaped morphology. Instead, uniformly high levels of stiffness across the dorsal forebrain lead to evagination. In contrast, the gain-of-function (GOF) of Cdh-2 leads to uniform actin accumulation, disrupting the normal apicobasal F-actin distribution required for localized flexibility and proper invagination.

Discussion

Morphogenesis of the forebrain roof plate is a classic example of how mechanical forces and molecular signaling converge to sculpt complex tissue architecture during development. This study establishes a mechanistic framework for forebrain roof plate morphogenesis by connecting cell adhesion dynamics, cortical tension regulation, and tissue-scale morphogenetic processes. Our findings reveal that, initially at HH18, the dorsal forebrain neuroepithelium exhibits a uniform stiffness of ~800 kPa and then undergoes dramatic remodeling by HH21 to establish a graded mechanical landscape, with the midline apex region becoming significantly more compliant at ~67 kPa, while the dorsolateral regions maintain an elevated stiffness of approximately 400 kPa. The gradual establishment of the 10-fold gradient of tissue stiffness parallels the morphological transformation of the relatively flat roof plate neuroepithelium to a complex W-shaped invagination. This mechanical patterning aligns with the established principles of epithelial morphogenesis, where differential tissue properties create the physical conditions necessary for controlled deformation. We also found that the mesenchymal tissue overlying the roof plate neuroepithelium maintained consistently high levels of stiffness, which increased dramatically to ~750 kPa in the region

above the midline vortex at HH23, when the W-shaped invagination became apparent. Moreover, our previous findings of differential cell proliferation across the forebrain roof plate neuroepithelium (*7*) imply that proliferating cells in the dorsolateral regions apply forces directed towards the midline. This force, coupled with the mechanical constraint created by the increasing stiffness of the overlying mesenchyme, enables the more compliant midline neuroepithelium to buckle inward rather than expanding outward. Such mechanical coupling between tissue layers has been demonstrated to be a fundamental mechanism in neural tube closure and other morphogenetic processes (*28*).

Classical cadherins have emerged as central mechanotransduction hubs that link extracellular mechanical cues to intracellular cytoskeletal reorganization. We discovered that a progressive increase in Cdh-2 protein localization along the apicobasal axis of the neuroepithelial cells in the roof plate midline mirrors the evolving changes in tissue stiffness and the morphological changes occurring in the dorsal forebrain. Functional perturbations revealed that Cdh-2 operates as a finely tuned mechanochemical rheostat rather than as a simple on/off switch. The loss-of-function of Cdh-2 results in uniformly elevated stiffness in the roof plate, leading to tissue evagination, whereas gain-of-function leads to a V-shaped invagination with altered mechanical properties. Interestingly, both perturbations abolished the normal stiffness gradient in the dorsal forebrain, demonstrating that the precise spatial and temporal regulation of Cdh-2 activity is required for proper morphogenesis. This finding is consistent with studies showing that cadherin-mediated mechanotransduction depends on the precise balance between adhesion and contractile forces (*29, 30*). Our discovery of negative feedback regulation controlling Cdh-2 levels during the development of the forebrain roof plate provides a mechanism for the dynamic self-regulation of these mechanical properties. Such feedback systems are essential for the maintenance of mechanical homeostasis during morphogenetic processes.

Through the assessment of cell proliferation, we found that changes in neuroepithelial stiffness and morphology of the dorsal forebrain upon manipulation of Cdh-2 are not the consequence of altered cell division; rather, the mechanical changes achieved are independent of proliferation dynamics. This supports an emerging paradigm in which biomechanical cues, integrated through cadherin-mediated adhesion and cytoskeletal remodeling, orchestrate developmental tissue patterning in concert with the classical

biochemical pathways. Our data implicate the adherens junction scaffolding protein ZO-1 as a critical mediator that links Cdh-2 to the cytoskeletal machinery. We observed that both loss and gain-of-function of Cdh-2 were accompanied by depletion of ZO-1, indicating a localized loss of junctional integrity. This finding is consistent with the findings of a recent study demonstrating that ZO-1 couples cadherin-catenin complexes to the actin cytoskeleton and modulates mechanical forces at apical adherens junctions. In endothelial cells, ZO-1 regulates tension acting on VE-cadherin-based adherens junctions and orchestrates spatial actomyosin organization (*31*).

The extension of mechanical signaling beyond apical junctions to influence apicobasal tissue properties suggests that Cdh-2 coordinates cortical actin dynamics throughout the length of the cell. Our analysis revealed that Cdh-2 perturbations dramatically altered F-actin distribution and accumulation along the apicobasal axis, consistent with models in which cadherin adhesion regulates cortical contractility through mechanisms such as adhesion signaling and mechanical coupling. Interestingly, the loss of Cdh-2 leads to the enhancement of apical F-actin accumulation and stiffness at later stages, which is paradoxical and is likely to be a result of compensatory cortical remodeling in response to junctional disruption rather than direct strengthening of mechanical coupling. The demonstration of negative feedback regulation of Cdh-2 expression further highlights the dynamic regulation of mechanical signaling during roof-plate morphogenesis. Similar phenomena have been observed in other epithelial contexts undergoing mechanical perturbation (*32, 33*). It has recently been reported that cortical actin organization is highly responsive to mechanical perturbation and can undergo rapid reorganization to maintain tissue integrity(*34-36*). Our findings elucidate a mechanochemical feedback loop, whereby Cdh-2 controls adherens junction stability and cortical actin architecture, generating spatially patterned stiffness gradients essential for neuroepithelial bending against a stiff mesenchymal scaffold. This study provides critical mechanistic insights into how heterogeneous mechanical microenvironments are established and coordinate morphogenetic processes in the developing brain.

This work has contributed significantly to the growing understanding of how cells generate and respond to mechanical forces during development. The identification of spatially graded mechanical properties as drivers of morphogenesis extends beyond the nervous system to other developing organ systems where

similar principles operate. The demonstration that differential adhesion and cortical contractility can be regulated independently through cadherin-mediated pathways provides mechanistic insights into the differential adhesion hypothesis, which has long been recognized as a fundamental principle governing cell sorting and tissue organization. Our findings suggest that cadherins regulate tissue mechanics through multiple pathways that can be independently modulated, allowing for fine-tuned control of morphogenetic processes. Future research integrating live force measurements and molecular dissection of Cdh-2-associated signaling complexes will be vital to fully unravel the intricate regulation of tissue mechanics during morphogenesis. Furthermore, exploring the roles of additional junctional components and mesenchymal factors will refine our understanding of the multi-tissue mechanical crosstalk that underpins epithelial folding.

In addition, this study has important implications for understanding developmental disorders such as holoprosencephaly (HPE), which in some cases results from failed invagination of the roof plate and consequent failure to divide the forebrain into cerebral hemispheres. Although genetic mutations in signaling molecules, such as sonic hedgehog, have been implicated in the etiology of HPE, the role of mechanical forces has received less attention. Our demonstration that Cdh-2-mediated mechanical regulation is essential for proper forebrain roof plate invagination suggests that perturbations in mechanotransduction pathways may contribute to HPE pathogenesis.

Materials and Methods

Chicken Eggs and Embryo Handling

Day old chicks of CARI PRIYA strain of the White Leghorn variety of chickens were procured from the Central Avian Research Institute, Izatnagar, Bareilly, Uttar Pradesh, India. These birds were maintained by Ganesh Enterprises in Nankari Village, Kanpur, Uttar Pradesh, India, and fertilized chicken eggs were procured from them. Eggs were incubated at 38 °C in a humidified incubator until the embryos reached the desired developmental stages, which was determined using the Hamburger and Hamilton staging system. Approval for conducting experiments with the fertilized chicken eggs was granted by the Animal Ethics

Committee, IIT Kanpur. Animal husbandry, supply, maintenance, and care in the animal facility before and during the experiments fully met the needs and welfare of animals.

Cell culture:

For the sensor assay, human embryonic kidney fibroblast cells (HEK293T) (ATCC, CRL3216) were transfected using Turbofect, according to the manufacturer's protocol.

Tissue Preparation for immunohistochemistry and RNA in situ hybridization

Heads were collected from both unmanipulated and electroporated embryos at the specified stages and fixed overnight in 4% paraformaldehyde (Catalog no. P6148, Sigma Aldrich). For cryoprotection, the samples were subjected to sucrose gradient immersion, first in 15% and then 30% sucrose solutions prepared in phosphate-buffered saline (PBS). Post-cryoprotection, the tissues were embedded in Polyfreeze/OCT compounds) and sectioned coronally at a thickness of 10 µm using a Leica CM1520 cryostat.

Tissue Preparation for AFM

Chick brain tissues were collected at appropriate developmental stages in Phosphate Buffered Saline (PBS). The tissues were then treated with 15% sucrose in 1X PBS for 4 h at 4°C, followed by 30% sucrose treatment for 4 h at RT. Afterward, the brains were embedded in Optimal Cutting Temperature compound (OCT/Polyfreeze) (Catalog no. P0019, Sigma Aldrich) and stored at -80°C. Cryosectioning was performed using a cryostat (Leica CM1850). Coronal sections, 2 µm thick, were placed on coverslips (Blue-Star, 22 × 22 mm) pre-coated with a 0.1% poly L-lysine solution.

Plasmids:

pCAG-dn-Cdh-2-IRES-GFP: The sequence of DNA provided below including EcoRI and NotI restriction sites was synthesized (Macrogen), followed by digestion with EcoRI and NotI restriction enzymes. To generate the CAG-IRES-GFP vector, the pCAG-NeuroD1-IRES-GFP plasmid (Add gene, 45025) was digested with EcoRI and NotI. The resulting restriction-digested synthesized DNA frag was ligated with the

digested vector using T4 DNA ligase, leading to the formation of pCAG-dn-Cdh-2- IRES-GFP. This was inspired by the dominant negative Cdh-2 construct described in literature (*20*).

Cdh-2 without extracellular domain (DNA)

5'ATGTGCCGGATAGCGGGAACGCCGCCGCGGATCCTGCCGCCGCTGGCGCTGATGCTGCTGGCGGCC
CTGCAGCAGGCACCGATAAAAGCAACTTGTGAAGACATGTTGTGCAAGATGGGATTTCCTGAAGATG
TGCACAGTGCAGTCGTGTCGAGGAGTGTACATGGAGGACAACCTCTGCTCAATGTGAGGTTTCAAAG
CTGCGATGAAAACAGAAAAATATACTTTGGAAGCAGTGAGCCAGAAGATTTTAGAGTAGGTGAAGA
TGGTGTGGTATATGCAGAGAGAAGCTTTCAACTTTCAGCAGAGCCCACGGAGTTTGTAGTGTCTGCT
CGAGACAAGGAAACTCAGGAAGAATGGCAAATGAAGGTGAAGCTACTGCAGCCTAATGCTATTAAC
ATCACTGCTGTAGACCCTGACATTGATCCAAATGCAGGCCCATTTGCCTTTGAGCTGCCTGATTCACC
TCCTAGTATTAAGAGGAATTGGACCATTGTTCGAATTAGTGGTGATCATGCCCAGCTCTCTTTAAGGA
TCAGGTTCCTGGAGGCTGGTATCTATGATGTGCCCATAGTAATTACAGATTCTGGAAATCCACATGCA
TCTAGCACTTCTGTGCTAAAAGTGAAAGTTTGCCAATGTGACATAAATGGGAGACTGTACTGATGTT
GACCGGATTGTTGGCGCAGGACTGGGCACTGGTGCCATCATTGCAATTCTGCTTTGTATCATCATCTT
ACTCATTTTAGTTTTGATGTTCGTAGTATGGATGAAGCGCCGTGATAAGGAGCGTCAGGCCAAGCAG
CTCTTAATTGATCCAGAAGATGATGTGAGGGACAACATTCTGAAATATGATGAAGAAGGTGGTGGAG
AAGAAGATCAGGATTATGACTTGAGCCAGCTCCAGCAGCCTGCACTGTAGAACCAGACGCCATCAA
ACCTGTTGGAATCAGACGTCTTGATGAAAGGCCAATCCATGCAGAACCTCAGTATCCAGTCAGATCA
GCTGCTCCTCATCCTGGGGACATTGGGGACTTCATTAATGAGGGACTTAAAGCAGCCGACAACGACC
CTACAGCCCCGCCATACGATTCCCTCTTAGTCTTTGACTATGAAGGAAGCGGCTCCACTGCTGGATCC
TTGAGCTCTCTTAATTCCTCAAGTAGCGGTGGTGAGCAAGACTATGACTACCTAAATGACTGGGGCC
CACGTTTCAAGAAACTTGCTGACATGTAGGTGGAGGTGATGACTGA3'

Full length Cdh-2:

This construction was provided by Prof. C. Cepko from Harvard Medical School, USA.

Sensor Assay:

To conduct the sensor assay, a Cdh-2-sensor construct was created and designated as pCAG a mCherry-Cdh-2-sensor. The 3' UTR of the chick Cdh-2 gene, which includes the target sequence for two Cdh-2 miRNAs, was PCR-amplified using the following primers:

Forward primer:

5′ATAGCGGCCGCTAGCACTTCAAAGTGAACTTTGTTTCTGG3′ (Not I)

Reverse primer:

5′GGCAAGCTTGTAGTCGACAATTTTCAGTCTCCTTATTTTAATAAAAGC3′(HindIII)

PCR amplification was performed using Phusion polymerase. The resulting amplified product was digested with NotI and HindIII restriction enzymes. This digested product was ligated into the pCAG-mCherry vector, which was also digested similarly. For the sensor assay, pCAG-mCherry-LacZ served as a negative control, as this construct did not contain Cdh-2 RNAi target sequences. Transfection included either pCAG-mCherry-Cdh-2-sensor or pCAG-mCherry-LacZ, alone or in combination with pRmiR-Cdh-2-RNAi-Oligo1 or pRmiR-Cdh-2-RNAi-Oligo2 at a molar ratio of 6:1. The transfection was done with HEK293T cells at 70% confluency. The expression of GFP or mCherry in transfected cells was subsequently observed. The mean fluorescence intensity was quantified using ImageJ software. An unpaired t-test was conducted using Origin Pro 2024b software to calculate the mean of all replicates, along with standard deviation (SD), standard error of the mean (SEM), and p-values.

In Ovo Electroporation

After 24 h of incubation, 3 ml of albumin was carefully removed to lower the embryo position inside the egg. A small window was then created on the eggshell above the forebrain vesicle at Hamburger-Hamilton stage 10 (HH10). DNA constructs (300ng to 1 µg/ml) mixed with 0.1% Fast Green (Catalog no. F7258, Sigma Aldrich) for visualization were injected into the forebrain vesicle. Electroporation was performed using platinum "hockey stick" electrodes (NepaGene, CUY611P3-1), positioned such that the positive electrode rested over the dorsal forebrain and the negative electrode beneath the yolk. Five 15 V square pulses, each

lasting 50 ms, were applied at 950 ms intervals, utilizing a BTX ECM830 electroporator (450662). After electroporation, sterile PBS containing penicillin and streptomycin was gently added to the embryos and the egg windows were sealed with tape. The eggs were returned to the incubator until the embryos reached the desired stages for tissue collection.

RNA In Situ Hybridization

Complementary DNA (cDNA) clones were used to generate digoxigenin labelled riboprobes for mRNA in situ hybridization. Antisense riboprobes were synthesized using appropriate RNA polymerases, such as T3 RNA polymerase (Catalog no. P2083, Promega), T7 RNA polymerase (Catalog no. P2075, Promega) or SP6 RNA polymerase (Catalog no. P4084, Promega). RNA in situ hybridization was conducted on coronal forebrain sections, following established methods (Trimarchi et al., 2007). Digoxigenin-labelled riboprobes for hybridization were synthesized via in vitro transcription of previously described cDNA clones.

Immunohistochemistry

Immunostaining of cryosections mounted on Poly-L-Lysine (Catalog no. P8920, Sigma Aldrich) coated slides involved three washes in PBS with 0.1% Tween-20 (PBT) for 10 min in PFA, followed by a 45 min block with 10% heat-inactivated goat serum in PBT. Primary antibodies were added to the blocking solution and incubated overnight at 4 °C. After washing three times with PBT for 5 min each, secondary antibodies (1:250) were incubated for 2 h at room temperature. Antibody used were Anti-N-Cadherin (Catalog no. C3865, Sigma-Aldrich), Anti-GFP (Catalog no. A-6455, ThermoFisher), Anti-phospho-Histone 3 (Catalog no. H0412, Sigma-Aldrich), Anti Zona occludens-1 (Catalog no. 61-7300, Invitrogen), Alexa Fluor 488-conjugated anti-mouse IgG (Catalog no.115-545-003, Jackson ImmunoResearch Labs), Alexa Fluor 594-conjugated anti-mouse IgG (Catalog no. 115-585-003, Jackson ImmunoResearch Labs), Alexa Fluor 594-conjugated anti-rabbit IgG (Catalog no.111-585-045, Jackson ImmunoResearch Labs), Alexa Fluor 488-conjugated anti-rabbit IgG (Catalog no. 111-545-003 , Jackson ImmunoResearch Labs), Phalloidin conjugated to Alexa Fluor 647 (Catalog no. A22287, ThermoFisher). For visualization of F-actin, the sections were incubated with phalloidin for 45 min at room temperature with 1% BSA (Hi Media MB083) in PBS. All sections were subsequently stained with DAPI (Catalog no. D9542-10MG, Sigma Aldrich) to mark nucleus.

Image Acquisition

Fluorescent images were captured using an AXR Nikon confocal microscope and a Carl Zeiss LSM780NLO multiphoton laser scanning confocal microscope, with accompanying software NIS Elements AR 5.42.04 and ZEN 2012 for image processing. RNA in situ hybridization images were obtained using a Leica DM500B stereomicroscope equipped with a DFC500 camera. The final image assembly and figure preparation were performed using Adobe Photoshop and Adobe Illustrator 2024.

Replicate definition

The experiments were performed with biological and technical replicates, as indicated. A biological replicate corresponded to one chicken embryo used for the experiment. Experiments with at least three biological replicates were used to calculate the statistical significance for each analysis. All graphs represent the mean ± SEM. All statistical analyses were performed, and graphs were generated using OriginPro software.

Quantification of Elastic Moduli

To calculate Young's modulus, an atomic force microscope (Oxford Instruments MFP3D origin) was used. Heat maps were generated with the help of Ms. Deepali Ubale, a technician at the Nanoscience Department of IIT Kanpur, India. Asylum Research Software was used to calculate Young's modulus. The Hertz model was used to generate heat maps. The probe used was from Oxford Instruments silicon probe with Au coating and a frequency of 100KHz was used. Spring Constant ≥ 0.3. The applied force was 10nN and the probe size was 10 nm. The Hertz model outlines the deformation characteristics of purely linearly elastic materials (Johnson et al., 1971). Therefore, when fitting any linear elastic data segment to the Hertz model for the modulus of elasticity (E), the resulting E will remain consistent across other linear elastic segments. Based on the comprehensive literature and derivation, the final Hertz equation for a spherical AFM tip is

$$F = \frac{4}{3} E^{*} R^{1/2} \delta^{3/2}$$

where:

F = Applied force (N)

E* = Reduced elastic modulus (Pa)

R = Radius of the spherical AFM tip (m)

δ = Indentation depth (m)

The reduced elastic modulus E* is defined as:

$$E^* = \frac{E}{1 - \upsilon^2}$$

where:

E = Young's modulus of the sample (Pa)

ν = Poisson's ratio of the sample

After generating the heat maps, we selected those with uniform colors and averaged them to determine the Young's modulus for 100 indentation points. For this analysis, three blocks (20 × 20 μm²) were scanned, each containing 100 points, with a focus on a specific region. This process was repeated for 6–8 embryos. Since tissue sections were embedded in OCT compound, we measured the stiffness of OCT alone without the embedded tissue, which yielded a value of 0.2 kPa. No linear relationship exists between OCT stiffness and tissue measurements. In the absence of a normalization formula to adjust for the effects of embedding the tissue in OCT, we plotted the raw stiffness values obtained from the spatial heat maps.

Quantification of Phalloidin Fluorescence Intensity

Phalloidin fluorescence intensity was quantified from the images acquired at 60X magnification. For each section, three distinct regions of interest (ROIs) were marked: midline apex, midline lateral, and dorsal lateral regions. Within each ROI, 30 lines were drawn, extending 80 μm from both the apical and basal surfaces of

neuroepithelial cells (indicated by red and green lines). Utilizing the 'Plot Profile' function in ImageJ software, fluorescence intensity profiles were generated along each line. The mean intensity values for each point across the lines are plotted for each ROI. To facilitate comparison, the intensity values were normalized to a range of 0–1 by dividing by 85 and plotted on the y-axis with the distance represented on the X-axis. This normalization was based on the maximum intensity value obtainable owing to the saturation limit of ImageJ, where 0 represents the lowest intensity and 1 represents the highest intensity. (N=3)

Quantification of PH3-Positive Cells

A rectangle measuring 375 µm × 375 µm was overlaid on the image at 40X magnification. The numbers of pH3 positive (red), GFP-positive (green), and double-positive (yellow) cells were counted manually using the ImageJ software. N=5 for midline and N=4 for lateral measurements

References

1. M. Valet, E. D. Siggia, A. H. Brivanlou, Mechanical regulation of early vertebrate embryogenesis. *Nature Reviews Molecular Cell Biology* **23**, 169-184 (2022).
2. H. Vignes, C. Vagena-Pantoula, J. Vermot, Mechanical control of tissue shape: Cell-extrinsic and -intrinsic mechanisms join forces to regulate morphogenesis. *Semin Cell Dev Biol* **130**, 45-55 (2022).
3. K. Chafiq, K. Toumi, F. E. Khayi, A. Daoudi, Alobar Holoprosencephaly in a Newborn: A Case Report of Prenatal Diagnosis and a Review of the Literature. *Cureus* **16**, e74462 (2024).
4. I. M. Orioli, E. E. Castilla, Epidemiology of holoprosencephaly: Prevalence and risk factors. *Am J Med Genet C Semin Med Genet* **154c**, 13-21 (2010).
5. V. Hamburger, H. L. Hamilton, A series of normal stages in the development of the chick embryo. 1951. *Dev Dyn* **195**, 231-272 (1992).

6. M. A. A. Zaidi, S. Kushwaha, N. Udaykumar, P. Dethe, M. Sachdeva, J. Sen, Interplay of canonical and LIMK mediated non-canonical BMP signaling is essential for regulating differential thickness and invagination during chick forebrain roof plate morphogenesis. *Dev Biol* **520**, 125-134 (2025).

7. S. Gupta, J. Sen, Retinoic acid signaling regulates development of the dorsal forebrain midline and the choroid plexus in the chick. *Development* **142**, 1293-1298 (2015).

8. G. L. Galea, Y. J. Cho, G. Galea, M. A. Molè, A. Rolo, D. Savery, D. Moulding, L. H. Culshaw, E. Nikolopoulou, N. D. E. Greene, A. J. Copp, Biomechanical coupling facilitates spinal neural tube closure in mouse embryos. *Proc Natl Acad Sci U S A* **114**, E5177-e5186 (2017).

9. M. Iwashita, N. Kataoka, K. Toida, Y. Kosodo, Systematic profiling of spatiotemporal tissue and cellular stiffness in the developing brain. *Development* **141**, 3793-3798 (2014).

10. M. S. Steinberg, Differential adhesion in morphogenesis: a modern view. *Current Opinion in Genetics & Development* **17**, 281-286 (2007).

11. L. Zhang, X. Wei, The Lego hypothesis of tissue morphogenesis: stereotypic organization of parallel orientational cell adhesions for epithelial self-assembly. *Biol Rev Camb Philos Soc* **100**, 445-460 (2025).

12. A. Ratheesh, A. S. Yap, A bigger picture: classical cadherins and the dynamic actin cytoskeleton. *Nature Reviews Molecular Cell Biology* **13**, 673-679 (2012).

13. R. Gong, M. J. Reynolds, X. Sun, G. M. Alushin, Afadin mediates cadherin-catenin complex clustering on F-actin linked to cooperative binding and filament curvature. *bioRxiv*, (2024).

14. S. Budnar, A. S. Yap, A mechanobiological perspective on cadherins and the actin-myosin cytoskeleton. *F1000Prime Rep* **5**, 35 (2013).

15. R. Winklbauer, Cell adhesion strength from cortical tension - an integration of concepts. *J Cell Sci* **128**, 3687-3693 (2015).

16. S. Moazzeni, K. Kyker-Snowman, R. I. Cohen, H. Wang, R. Li, D. I. Shreiber, J. D. Zahn, Z. Shi, H. Lin, N-Cadherin based adhesion and Rac1 activity regulate tension polarization in the actin cortex. *Scientific Reports* **15**, 4296 (2025).

17. N. Udaykumar, M. A. A. Zaidi, A. Rai, J. Sen, CNKSR2, a downstream mediator of retinoic acid signaling, modulates the Ras/Raf/MEK pathway to regulate patterning and invagination of the chick forebrain roof plate. *Development* **150**, (2023).

18. Z. Liu, J. L. Tan, D. M. Cohen, M. T. Yang, N. J. Sniadecki, S. A. Ruiz, C. M. Nelson, C. S. Chen, Mechanical tugging force regulates the size of cell-cell junctions. *Proc Natl Acad Sci U S A* **107**, 9944-9949 (2010).

19. R. M. Mège, N. Ishiyama, Integration of Cadherin Adhesion and Cytoskeleton at Adherens Junctions. *Cold Spring Harb Perspect Biol* **9**, (2017).

20. C. Kintner, Regulation of embryonic cell adhesion by the cadherin cytoplasmic domain. *Cell* **69**, 225-236 (1992).

21. L. L. Ong, N. Kim, T. Mima, L. Cohen-Gould, T. Mikawa, Trabecular myocytes of the embryonic heart require N-cadherin for migratory unit identity. *Dev Biol* **193**, 1-9 (1998).

22. C. A. Smith, K. N. Roeszler, T. Ohnesorg, D. M. Cummins, P. G. Farlie, T. J. Doran, A. H. Sinclair, The avian Z-linked gene DMRT1 is required for male sex determination in the chicken. *Nature* **461**, 267-271 (2009).

23. E. Méhes, T. Vicsek, Collective motion of cells: from experiments to models. *Integrative Biology* **6**, 831-854 (2014).

24. A. S. Fanning, C. M. Van Itallie, J. M. Anderson, Zonula occludens-1 and -2 regulate apical cell structure and the zonula adherens cytoskeleton in polarized epithelia. *Mol Biol Cell* **23**, 577-590 (2012).

25. M. Itoh, A. Nagafuchi, S. Moroi, S. Tsukita, Involvement of ZO-1 in cadherin-based cell adhesion through its direct binding to alpha catenin and actin filaments. *J Cell Biol* **138**, 181-192 (1997).

26. J. L. Maiers, X. Peng, A. S. Fanning, K. A. DeMali, ZO-1 recruitment to α-catenin--a novel mechanism for coupling the assembly of tight junctions to adherens junctions. *J Cell Sci* **126**, 3904-3915 (2013).

27. Q. Yu, W. R. Holmes, J. P. Thiery, R. B. Luwor, V. Rajagopal, Cortical tension initiates the positive feedback loop between cadherin and F-actin. *Biophysical Journal* **121**, 596-606 (2022).

28. N. Christodoulou, P. A. Skourides, Distinct spatiotemporal contribution of morphogenetic events and mechanical tissue coupling during Xenopus neural tube closure. *Development* **149**, (2022).

29. J. L. Maître, C. P. Heisenberg, Three functions of cadherins in cell adhesion. *Curr Biol* **23**, R626-633 (2013).

30. A. F. Mertz, Y. Che, S. Banerjee, J. M. Goldstein, K. A. Rosowski, S. F. Revilla, C. M. Niessen, M. C. Marchetti, E. R. Dufresne, V. Horsley, Cadherin-based intercellular adhesions organize epithelial cell–matrix traction forces. *Proceedings of the National Academy of Sciences* **110**, 842-847 (2013).

31. O. Tornavaca, M. Chia, N. Dufton, L. O. Almagro, D. E. Conway, A. M. Randi, M. A. Schwartz, K. Matter, M. S. Balda, ZO-1 controls endothelial adherens junctions, cell-cell tension, angiogenesis, and barrier formation. *J Cell Biol* **208**, 821-838 (2015).

32. J. X. H. Li, V. W. Tang, W. M. Brieher, Actin protrusions push at apical junctions to maintain E-cadherin adhesion. *Proc Natl Acad Sci U S A* **117**, 432-438 (2020).

33. M. V. Rao, R. Zaidel-Bar, Formin-mediated actin polymerization at cell-cell junctions stabilizes E-cadherin and maintains monolayer integrity during wound repair. *Mol Biol Cell* **27**, 2844-2856 (2016).

34. H. De Belly, O. D. Weiner, Follow the flow: Actin and membrane act as an integrated system to globally coordinate cell shape and movement. *Current Opinion in Cell Biology* **89**, 102392 (2024).

35. R. Sakamoto, D. S. Banerjee, V. Yadav, S. Chen, M. L. Gardel, C. Sykes, S. Banerjee, M. P. Murrell, Membrane tension induces F-actin reorganization and flow in a biomimetic model cortex. *Communications Biology* **6**, 325 (2023).

36. J. Hu, S. Chen, W. Hu, S. Lü, M. Long, Mechanical Point Loading Induces Cortex Stiffening and Actin Reorganization. *Biophys J* **117**, 1405-1418 (2019).

Acknowledgments

The authors acknowledge Prof. Constance Cepko (Harvard Medical School, Boston, MA, USA) for the Cdh-2 FL (chick). The authors acknowledge Deepali Ubale for help with atomic force microscopy and force mapping and the Department of Nanoscience at IIT Kanpur for the AFM facility. Th The authors acknowledge Ms. Neetu Dey for help with the multiphoton laser scanning confocal microscope. The authors acknowledge Ms. Rashmi Parihar for help with generation of 2 µm cryosection at the cryo-sectioning facility at CEAF, IIT Kanpur. The authors are grateful to Dr. Sandeep Gupta, Dr. Tathagata Biswas, and Prof. Amitabha Bandyopadhyay for critical comments on the manuscript. The authors acknowledge Mr. Naresh Gupta for technical support in this study.

Funding:

This study was supported by a grant from the Department of Biotechnology (DBT), Government of India (BT/PR42304/MED/97/613/2021) to J.S. and M. S., P.S., S.K., P.G. and M.A.A.Z. are supported by the Ministry of Human Resources and Development (MHRD), Government of India, for their PhD fellowship.

Author contributions:

Conceptualization: M.S, J.S Methodology: M.S., P.S., P.G., M.A.A.Z., S.K. and J.S. Software: M.S. Formal Analysis: M.S, J.S. Investigation: M.S, J.S. Resources: J.S. Data Curation: M.S., J.S. Visualization: M.S., S.K., J.S. Supervision: J.S. Writing original draft: M.S., J.S. Writing & editing: M.S., P.G., J.S. Project administration: J.S. Funding acquisition: J.S.

Competing interests:

The authors declare no competing or financial interests.

Data and materials availability:

The construct expressing dominant negative CDH-2 and CDH-2 RNAi generated during this study will be shared upon coverage of shipping costs. The detailed protocol for measuring the stiffness of the embryonic forebrain tissues of *Gallus gallus* would also be shared upon request.

No standardized data types were generated in this study. All data supporting the conclusions can be found in the main text or are available upon request from the corresponding author. Any additional information required to reanalyze the data reported in this study is available from the lead contact upon request. Requests for further information and resources should be directed to and will be fulfilled by the lead contact, Jonaki Sen (jonaki@iitk.ac.in)

Figures

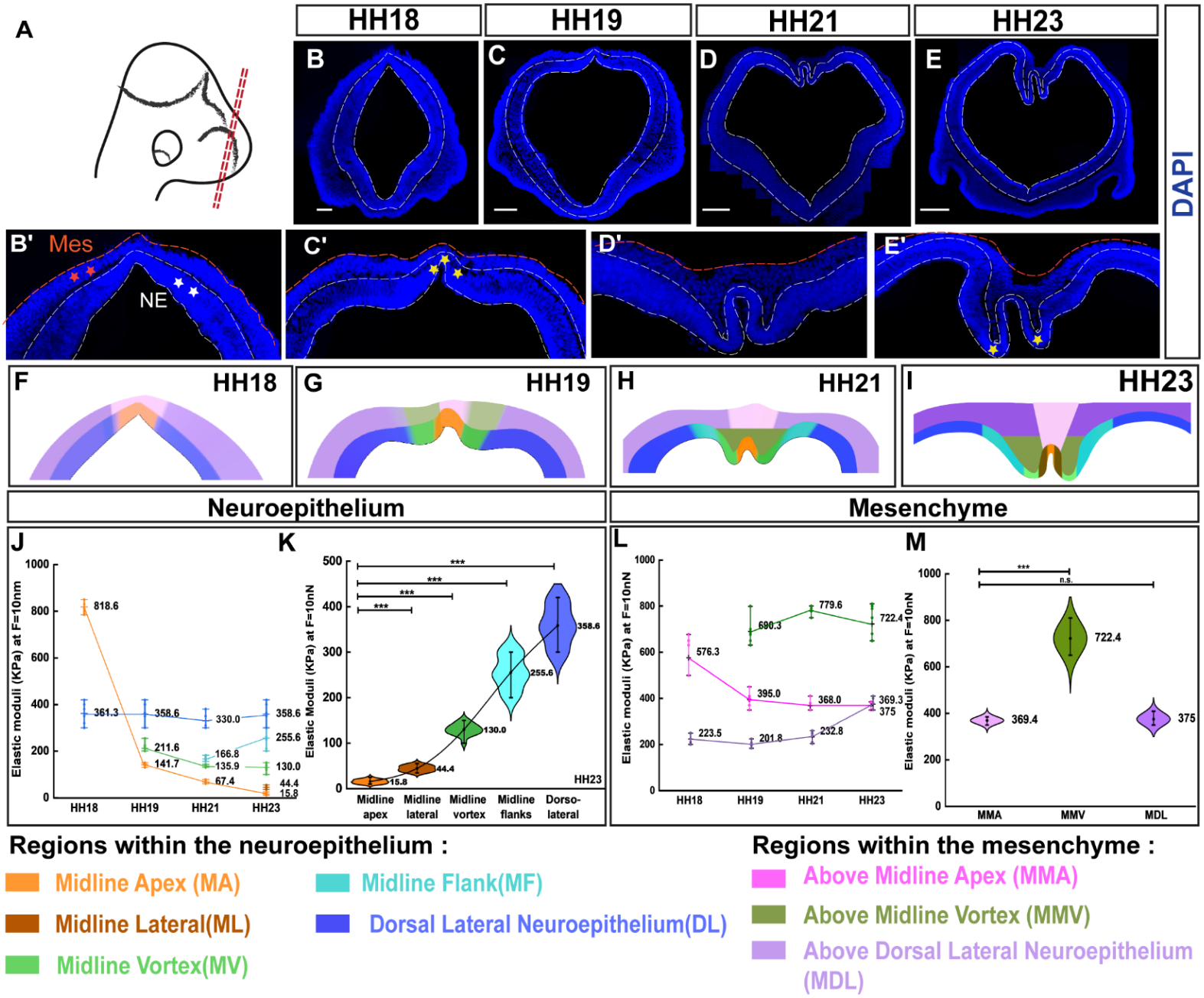

Fig.1. Spatiotemporal changes in tissue stiffness of the neuroepithelium and mesenchyme during dorsal forebrain morphogenesis.

(A) A schematic illustration of the head of a chick embryo with the dashed red lines indicated the plane of sectioning of the forebrain. Coronal sections were taken from the mid-anterior to mid-posterior regions of the chick forebrain.

(B, C, D, E) Images of DAPI-stained coronal sections from the mid-posterior region of the chick forebrain at various developmental stages from HH18 to HH23, 20X magnification; the white dashed line demarcates the neuroepithelium. Scale bar: 100µm

(B′, C′, D′, E′) High magnification images of the DAPI stained dorsal forebrain sections at different stages of development from HH18 to HH23. The neuroepithelium is denoted by the white dashed line and asterisks, while the

mesenchyme is represented by the red line and red asterisks. Yellow asterisks mark the “pucker” at HH19 (C’) and midline vortex at HH23 (E’).

(F, G, H, I) Schematic of the dorsal forebrain at stages HH18, HH19, HH21 and HH23 with distinct colours marking subdomains of the roof plate neuroepithelium and overlying mesenchyme. The colour code for each subdomain is provided at the bottom.

(J) The change in stiffness of different subdomains of the neuroepithelium plotted across developmental time. Each coloured line represents a distinct subdomain of the neuroepithelium. (N=5)

(K) Violin plots of the stiffness of each subdomain of the neuroepithelium at HH23 (colour coded in I), with mean values and SEM indicated (N=8). The stiffness of the midline apex (MA) significantly different from other subdomains (p-value ≤ 0.001).

(L) The change in stiffness of different subdomains of the dorsal mesenchyme plotted across developmental time. Each colored line represents a distinct subdomain of the mesenchyme. (N=5)

(M) Violin plots of the stiffness of each subdomain of the dorsal mesenchyme at HH23 (colour coded in I), with mean values and SEM indicated (N=8). The stiffness of the mesenchyme above midline apex (MMA) is significantly different from that above the midline vortex (MMV) (p-value ≤ 0.001).

Two-way ANOVA was used for statistical analysis, followed by Tukey's post-hoc analysis (K,M), with the p-values indicated.

See also Fig. S1.

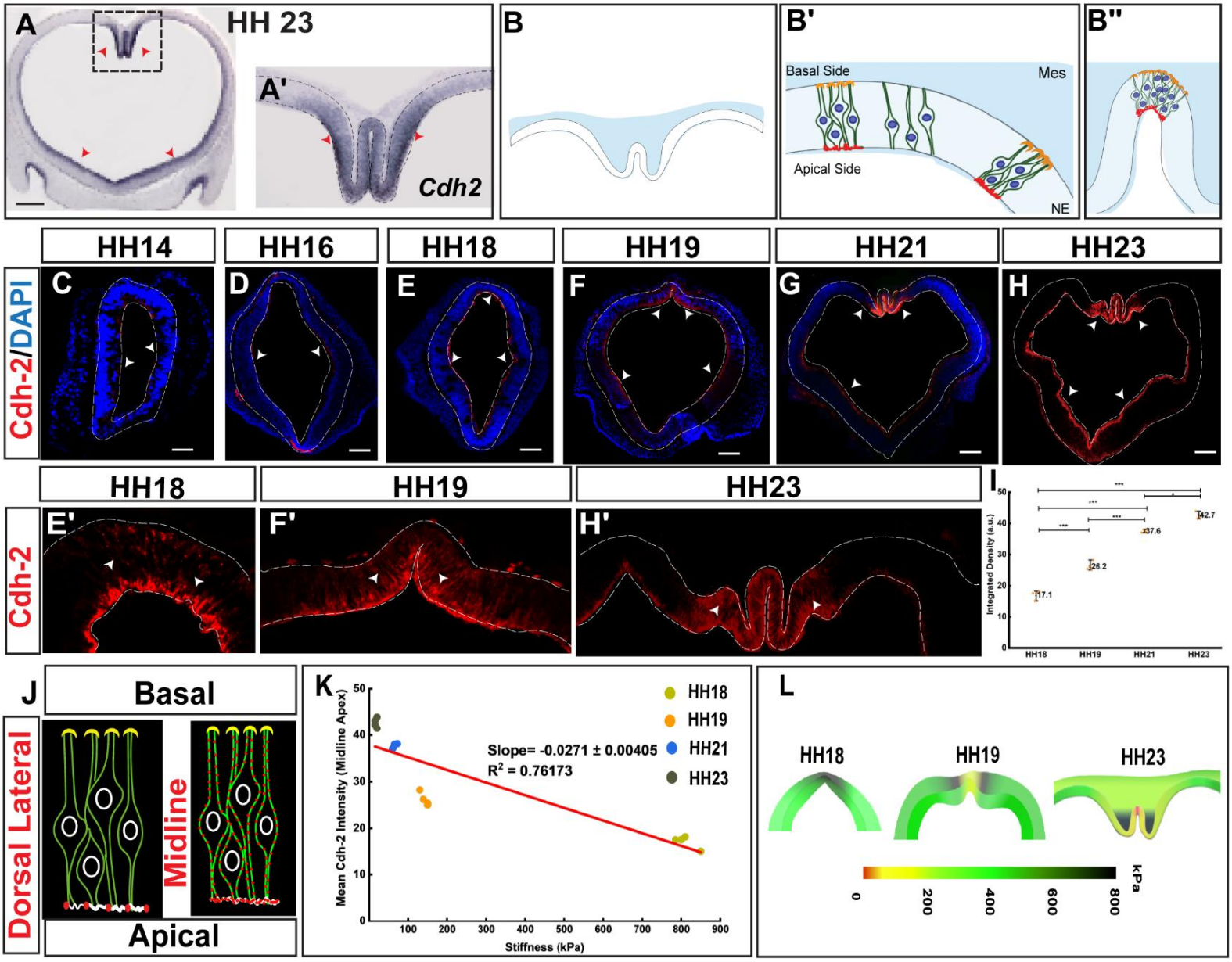

Fig. 2. The dynamics of Cdh-2 expression correlate with stiffness changes during forebrain morphogenesis.

(A) Sections of the chick forebrain at HH23 showing mRNA expression of *Cdh2.* The red arrowheads indicate domains where *Cdh2* expression is relatively high. Scale bar: 100 µm. (A′) High magnification image of the forebrain midline region at HH23 shown in the boxed region of (A).

(B) A schematic representation of the dorsal forebrain neuroepithelium, the apical (red circles) and basal (orange circles) sides are indicated.

(B') A schematic representation of the pseudostratified neuroepithelium with every cell spanning the apical to the basal side and nuclei located at distinct depths.

(B") A schematic representation of the pseudostratified neuroepithelium depicting the decrease in thickness from the dorsal lateral region to the midline of the roof plate.

(C, D, E, F, H) Immunohistochemical detection of Cdh-2 in sections of the forebrain at different stages from HH14 (embryonic day 2) to HH23 (embryonic day 3.5). (C, D, E, F) DAPI (blue) and Cdh-2 (red) merged image of the section of chick forebrain from HH14 to HH21. (H) Image of a section of the chick forebrain at HH23 with Cdh-2 (red) immunostaining. A white arrow marks the region of high expression. Scale bar: 100 µm.

(E', F', H') High magnification images of sections of the dorsal forebrain with Cdh-2 immunostaining (red) at HH18, HH19, and HH23.

(I) The change in the intensity of Cdh-2 staining in the roof plate midline plotted across developmental time (HH18 to HH23) (N=4). Significance of difference in Cdh-2 staining between stages assessed by unpaired t-test using Origin 2024b ($p \leq 0.001$).

(J) Schematic representation of distribution of Cdh-2 protein across the apicobasal axis of neuroepithelial cells in the roof plate midline and dorsal-lateral regions of the forebrain. The neuroepithelial cell membrane is coloured green and Cdh-2 protein is denoted by red circles.

(K) Regression analysis curve depicting correlation between the change in Cdh-2 intensity and the change in stiffness over time at the midline apex region using Origin 2024b. (N=4)

(L) Schematic illustration depicting the variation in stiffness (using a colour code) across different subdomains of the neuroepithelium and mesenchyme of the dorsal forebrain, during the invagination process at embryonic stages HH18, HH19, and HH23.

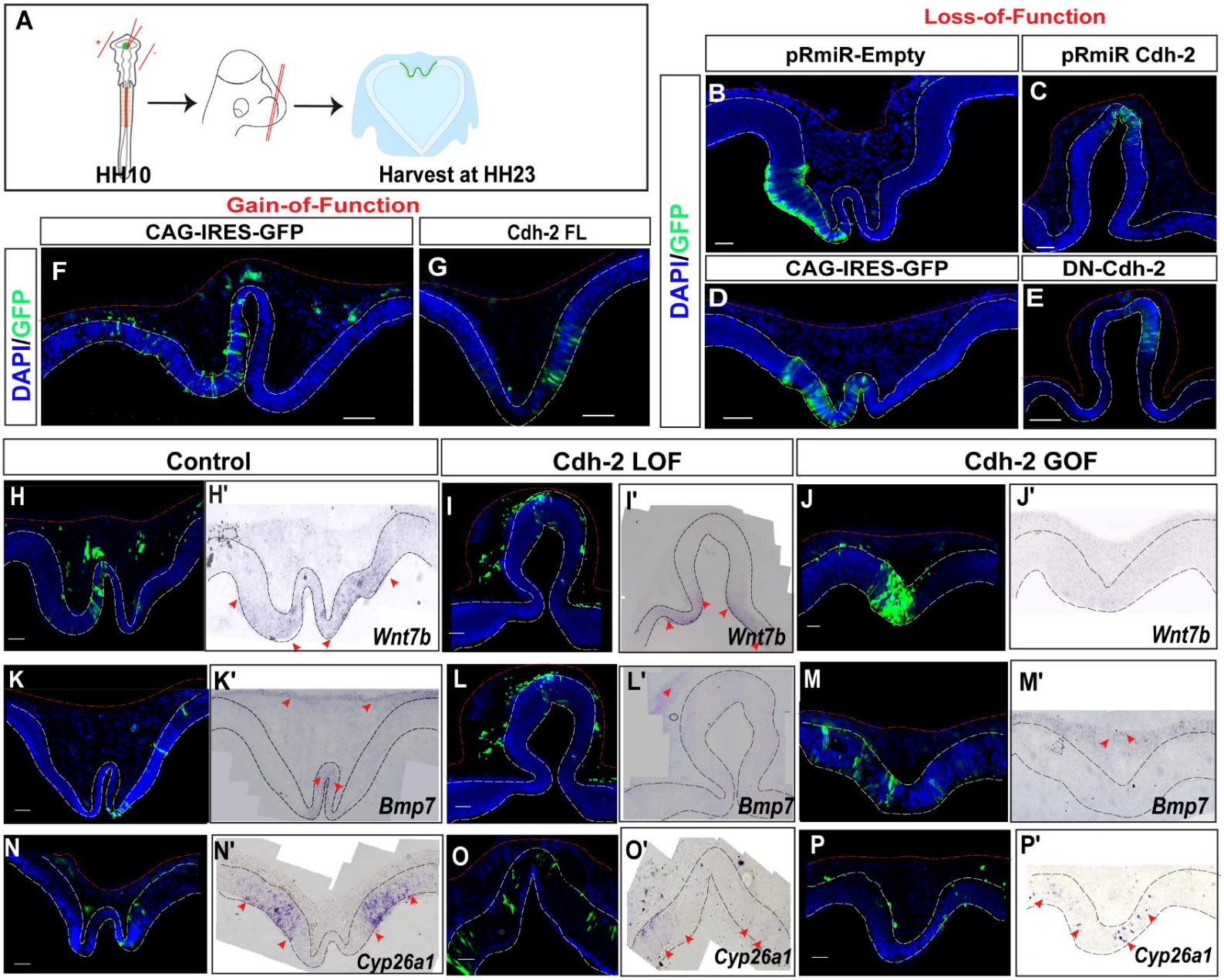

Fig. 3. Disruption of Cdh-2 function impairs patterning of the roof plate.

(A) Schematic of experimental design for generating LOF of Cdh-2 through electroporation of construct expressing dnCdh-2 or RNAi targeting Cdh-2 and GOF of Cdh-2 through electroporation of construct expressing Cdh-2 FL.

(B, C) Images of DAPI stained sections of the forebrain roof plate of the chick embryo electroporated with control construct, pRmiR empty (B) and pRmiR-Cdh-2 RNAi (C) for LOF of Cdh-2. Green fluorescence marks the domain of electroporation. Scale bar: 100 µm.

(D, E) Images of DAPI stained sections of the forebrain roof plate of the chick embryo electroporated with control construct, CAG-IRES-GFP (D) and pCAG-DN-Cdh2 (E) for LOF of Cdh-2. Green fluorescence marks the domain of electroporation. Scale bar: 100 µm.

(F, G) Images of DAPI stained sections of the forebrain roof plate of the chick embryo electroporated with control construct, CAG-IRES-GFP (F) and pCAG- Cdh2-FL (G) for GOF of Cdh-2. Green fluorescence marks the domain of electroporation. Scale bar: 100 µm.

(H, K, N) Images of DAPI stained sections of the chick forebrain roof plate at HH23 electroporated with the control construct pCAG-GFP. Green fluorescence indicates the extent of electroporation. (H', K', N') Images of the chick forebrain roof plate at HH23 electroporated with the control construct pCAG-GFP with expression of *Wnt7b* (H'), *Bmp7* (K'), and *Cyp26a1*(N') mRNA indicated by the purple-blue colour. Red arrows demarcate the domains of expression. Scale bar: 100 µm (N=3).

(I, L, O) Images of DAPI stained sections of the chick forebrain roof plate at HH23 electroporated with the construct pCAG-DN-Cdh-2. Green fluorescence indicates the extent of electroporation. (I', L', O') Images of the chick forebrain roof plate at HH23 electroporated with the construct pCAG-DN-Cdh-2 showing expression of *Wnt7b* (I'), *Bmp7* (L'), and *Cyp26a1*(O') mRNA indicated by the purple-blue colour. Red arrows demarcate the domains of expression. Scale bar: 100 µm (N=3).

(J, M, P) Images of DAPI stained sections of the chick forebrain roof plate at HH23 electroporated with the construct pCAG-Cdh-2-FL. Green fluorescence indicates the extent of electroporation. (J', M', P') Images of the chick forebrain roof plate at HH23 electroporated with the construct p-CAG- Cdh-2-FL showing expression of *Wnt7b* (J'), *Bmp 7* (M'), and *Cyp26a1* (P') mRNA indicated by the purple-blue colour. Red arrows demarcate the domains of expression. Scale bar: 100 µm (N=3).

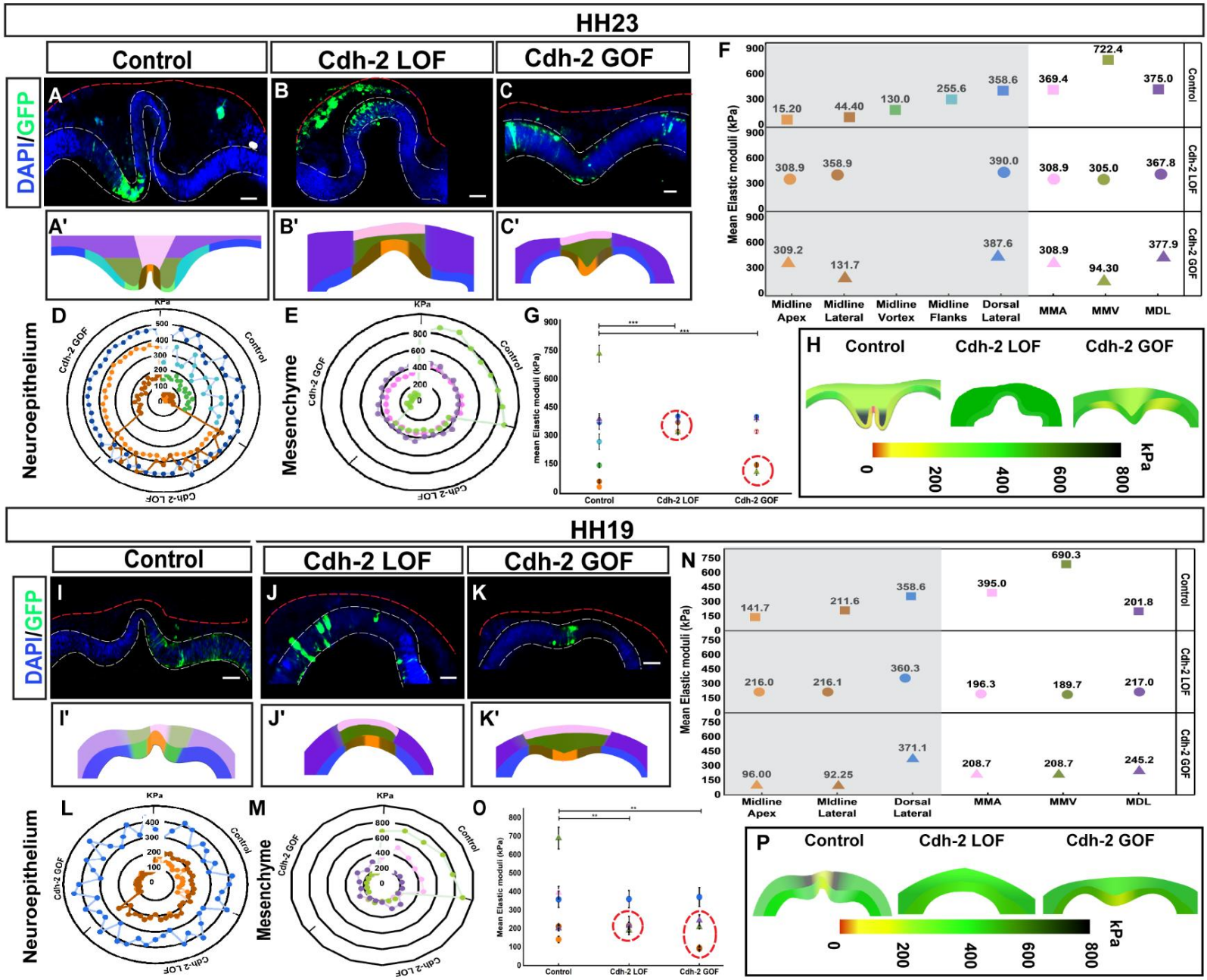

Fig. 4. Modulation of Cdh-2 alters the stiffness of the neuroepithelium and overlying mesenchyme in the dorsal forebrain.

(A, B, C) Images of DAPI stained sections of the chick forebrain roof plate at HH23 electroporated with control (pCAG-GFP), Cdh-2 LOF (pCAG-DN-Cdh-2) and Cdh-2 GOF (pCAG-Cdh-2-FL), respectively, the white dashed line demarcates the neuroepithelium Scale bar: 100 µm.

(A', B', C') A schematic representation of the chick forebrain roof plate at HH23 electroporated with control (A'), Cdh-2 LOF (B') and Cdh-1 GOF (C'). The subdomains of the neuroepithelium and mesenchyme that were probed with AFM for measuring stiffness are denoted in different colours.

(D) The radar plot comparing the stiffness of the roof plate neuroepithelium at HH23 in the control, Cdh-2 LOF and Cdh-2 GOF electroporated forebrains. Each dot represents the mean of the 100 points of region of interest (ROI) as shown in Fig. S6.

(E) The radar plot comparing the stiffness of the dorsal mesenchyme at HH23 in the control, Cdh-2 LOF and Cdh-2 GOF electroporated forebrains. Each dot represents the mean of the 100 points of each region of interest (ROI) as shown in Fig. S6.

(F) The scatter plot for the mean stiffness of each ROI of the roof plate neuroepithelium (grey shaded region) and the dorsal mesenchyme (unshaded region) at HH23 of control, Cdh-2 LOF, and Cdh-2 GOF electroporated forebrains. Each dot represents the mean of the 100 points of each region of interest (ROI) as shown in Fig. S6.

(G) The dot plot for the mean stiffness (Mean ± SEM) of each ROI of the roof plate neuroepithelium (grey shaded region) and the dorsal mesenchyme (unshaded region) at HH23 of control, Cdh-2 LOF, and Cdh-2 GOF electroporated forebrains. Colour coded circles and triangles represent each ROI in the neuroepithelium and mesenchyme, respectively. Each circle/triangle represents the mean of the 100 points within each region of interest (ROI) as shown in Fig. S6. Red dashed circles indicate the distribution of the mean stiffness across the subdomains of the roof plate neuroepithelium and the dorsal mesenchyme. Unpaired t-test using Origin 2024b was used to determine significance $p \leq 0.001$. (N=4).

(H) Schematic depicting the variation in stiffness (using a colour code) across different subdomains of the neuroepithelium and mesenchyme of the dorsal forebrain, upon Cdh-2 perturbation, during the invagination process at HH23.

(I, J, K) Images of DAPI stained sections of the chick forebrain roof plate at HH19 electroporated with control (pCAG-GFP), Cdh-2 LOF (pCAG-DN-Cdh-2) and Cdh-2 GOF (pCAG-Cdh-2-FL), respectively, the white dashed line demarcates the neuroepithelium Scale bar: 100 µm.

(I', J', K') A schematic representation of the chick forebrain roof plate at HH19 electroporated with control (I'), Cdh-2 LOF (J') and Cdh-1 GOF (K'). The subdomains of the neuroepithelium and mesenchyme that were probed with AFM for measuring stiffness are denoted in different colours.

(L) The radar plot comparing the stiffness of the roof plate neuroepithelium at HH19 in the control, Cdh-2 LOF and Cdh-2 GOF electroporated forebrains. Each dot represents the mean of the 100 points of region of interest (ROI) as shown in Fig. S7.

(M) The radar plot comparing the stiffness of the dorsal mesenchyme at HH19 in the control, Cdh-2 LOF and Cdh-2 GOF electroporated forebrains. Each dot represents the mean of the 100 points of each region of interest (ROI) as shown in Fig. S7.

(N) The scatter plot for the mean stiffness of each ROI of the roof plate neuroepithelium (grey shaded region) and the dorsal mesenchyme (unshaded region) at HH19 of control, Cdh-2 LOF, and Cdh-2 GOF electroporated forebrains. Each dot represents the mean of the 100 points of each region of interest (ROI) as shown in Fig. S7.

(O) The dot plot for the mean stiffness (Mean ± SEM) of each ROI of the roof plate neuroepithelium (grey shaded region) and the dorsal mesenchyme (unshaded region) at HH19 of control, Cdh-2 LOF, and Cdh-2 GOF electroporated forebrains. Colour coded circles and triangles represent each ROI in the neuroepithelium and the mesenchyme, respectively. Each circle/triangle represents the mean of the 100 points within each region of interest (ROI) as shown in Fig. S7. Red dashed circles indicate the distribution of the mean stiffness of subdomains of the roof plate neuroepithelium and the dorsal mesenchyme. Unpaired t-test using Origin 2024b was used to determine significance $p \leq 0.001$. ($N = 4$).

(P) Schematic depicting the variation in stiffness (using a colour code) across different subdomains of the neuroepithelium and mesenchyme of the dorsal forebrain, upon Cdh-2 perturbation, during the invagination process at HH19.

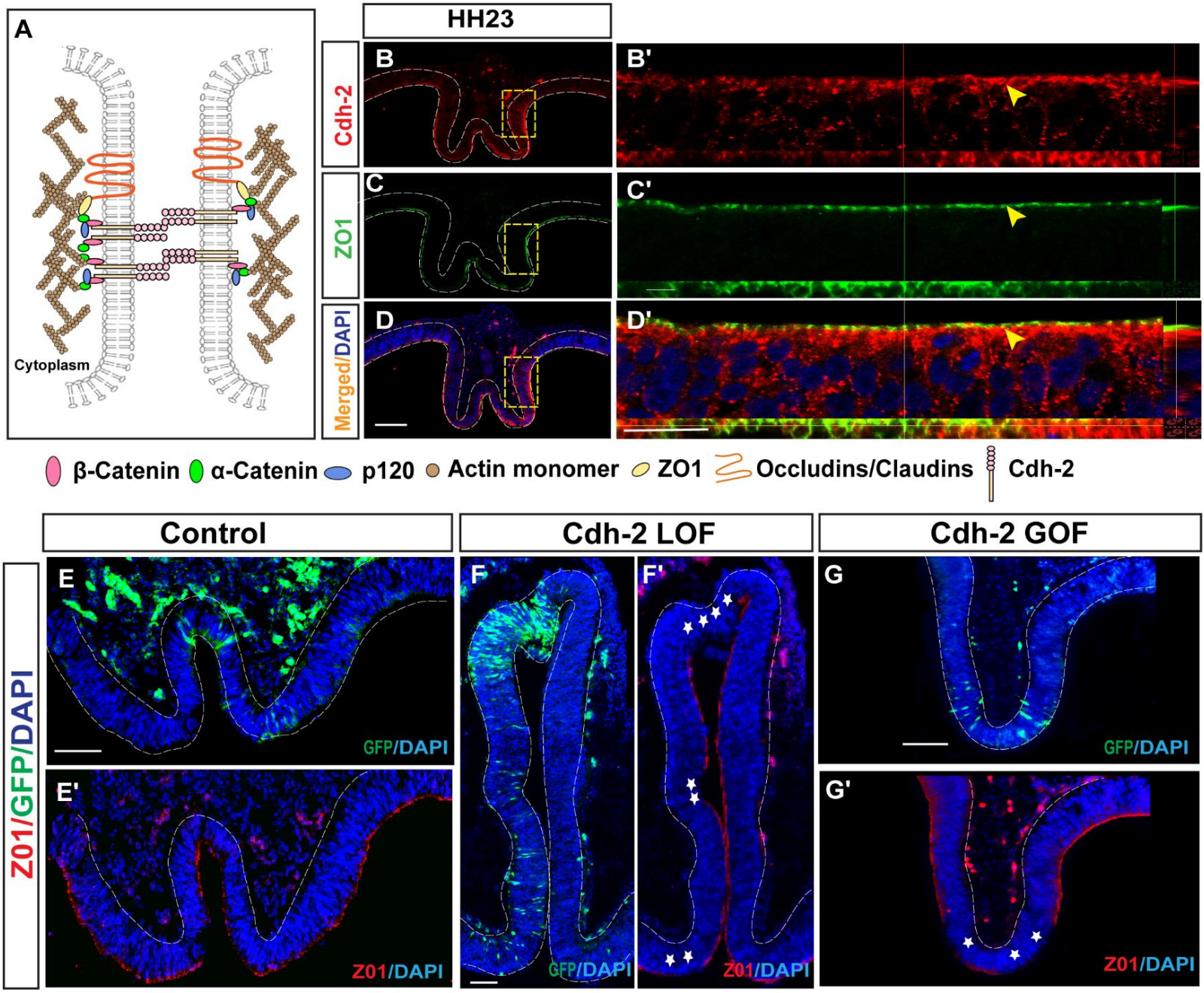

Fig. 5. Functional manipulation of Cdh-2 disrupts the integrity of adherens junctions.

(A) Schematic representation of adherence junction showing the ZO-1 and Cdh-2 and their interaction with the actin cytoskeleton.

(B) Image of the section of the chick forebrain at HH23 with Cdh-2 immunohistochemistry (Red). White dashed line demarcates the neuroepithelium and yellow dashed box encloses the region of interest from which the high magnification (60X) image has been captured. Scale bar: 100µm.

(B') A frame from the images taken with a confocal microscope from the region within the yellow dashed box with Cdh-2 immunohistochemistry (red). Yellow arrow indicates the apical surface with Cdh-2 distribution.

(C) Image of the section of the chick forebrain at HH23 with ZO-1 immunohistochemistry (green). White dashed line demarcates the neuroepithelium and yellow dashed box encloses the region of interest from which the high magnification (60X) image has been captured. Scale bar: 100µm

(C') A frame from the images taken with a confocal microscope from the region within the yellow dashed box with ZO-1 immunohistochemistry (green). Yellow arrow indicates the apical surface with ZO-1 distribution.

(D) Merged Image of the section of the chick forebrain at HH23 with Cdh-2 (Red) and ZO-1(green) immunohistochemistry and DAPI stained nuclei (blue). White dashed line demarcates the neuroepithelium and yellow dashed box encloses the region of interest from which the high magnification (60X) image has been captured. Scale bar: 100µm

(D') A frame from the images taken with a confocal microscope from the region within the yellow dashed box with merged Cdh-2 (red) and ZO-1 (green) immunohistochemistry and DAPI stained nuclei (blue). Yellow arrow indicates the apical surface with Cdh-2 and ZO-1 distribution. Scale bar: 100µm

(E) Image of DAPI-stained (blue) section of the chick forebrain electroporated with the control construct (pCAG-IRES-GFP), where green fluorescence demarcates the domain of electroporation. Scale bar: 100µm

(E′) Image of a DAPI-stained (blue) section of the chick forebrain electroporated with the control construct (pCAG-IRES-GFP), with ZO1 immunohistochemistry (red).

(F) Image of DAPI-stained (blue) section of the chick forebrain electroporated with the Cdh-2 LOF construct (pCAG-DN-Cdh-2), where green fluorescence demarcates the domain of electroporation. Scale bar: 100µm

(F′) Image of a DAPI-stained (blue) section of the chick forebrain electroporated with the Cdh-2 LOF construct (pCAG-DN-Cdh-2), with ZO1 immunohistochemistry (red). White stars indicate regions with loss of ZO1.

(G) Image of DAPI-stained (blue) section of the chick forebrain electroporated with the Cdh-2 GOF construct (pCAG-Cdh-2-FL), where green fluorescence demarcates the domain of electroporation. Scale bar: 100µm

(G′) Image of a DAPI-stained (blue) section of the chick forebrain electroporated with the Cdh-2 GOF construct (pCAG-Cdh-2-FL), with ZO1 immunohistochemistry (red). White stars indicate region with loss of ZO1. Scale bar = 100 µm

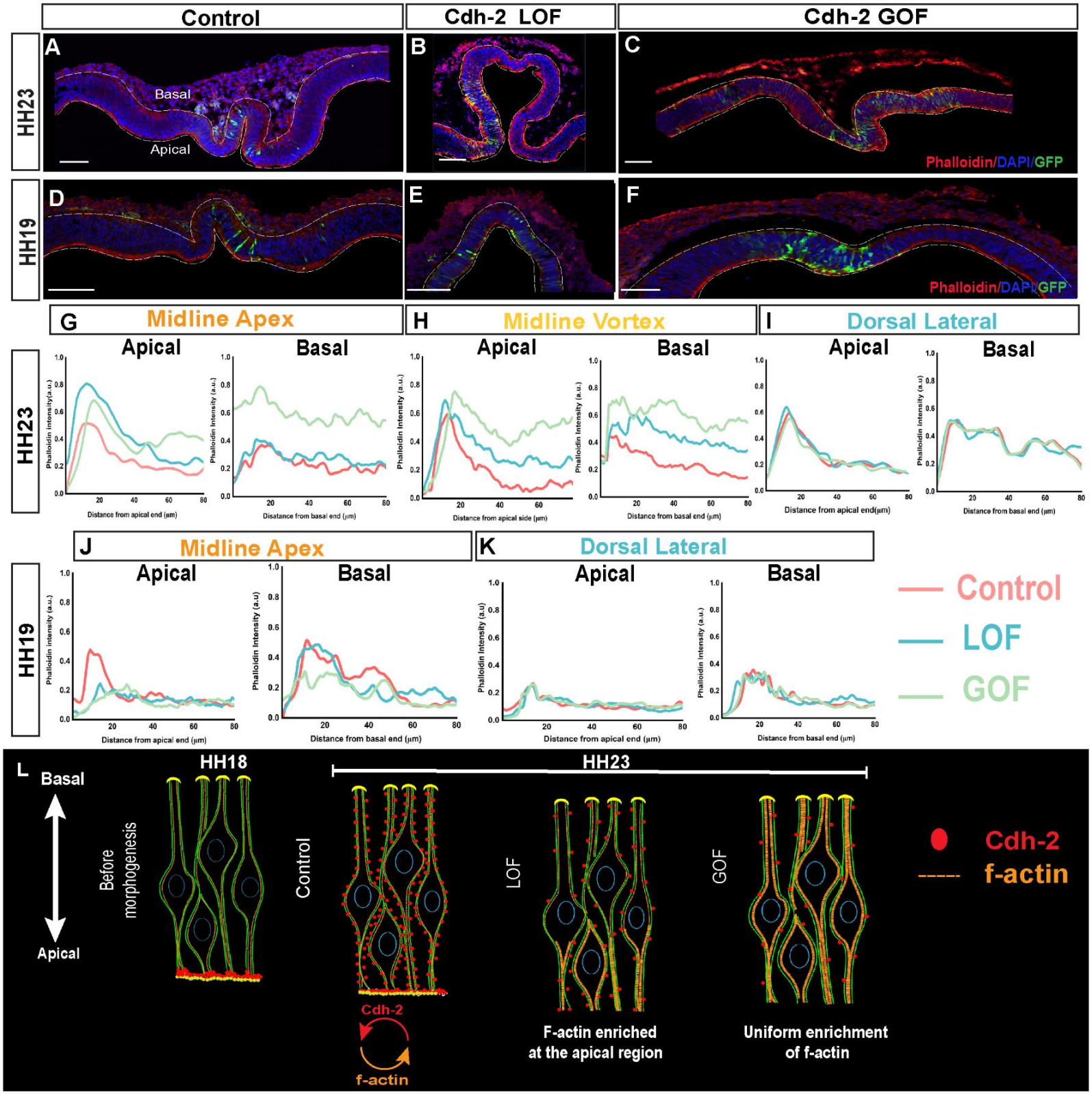

Fig. 6. Cdh-2 regulates the spatial distribution of cortical F-actin in the roof plate neuroepithelial cells.

(A) The merged image of a section of the control (pCAG-GFP) electroporated dorsal forebrain region at HH23, with DAPI (blue) marking the nuclei of neuroepithelial cells, phalloidin (red) marking the cortical actin within cells, and green marking the electroporated cells. Scale bar: 100 µm.

(B) The merged image of a section of the Cdh-2 LOF (pCAG-DN-Cdh-2) electroporated dorsal forebrain region at HH23, with DAPI (blue) marking the nuclei of neuroepithelial cells, phalloidin (red) marking the cortical actin within cells, and green marking the electroporated cells. Scale bar: 100 µm.

(C) The merged image of a section of the Cdh-2 GOF (pCAG-Cdh-2-FL) electroporated dorsal forebrain region at HH23, with DAPI (blue) marking the nuclei of neuroepithelial cells, phalloidin (red) marking the cortical actin within cells, and green marking the electroporated cells. Scale bar: 100 µm.

(D) The merged image of a section of the control (pCAG-GFP) electroporated dorsal forebrain region at HH19, with DAPI (blue) marking the nuclei of neuroepithelial cells, phalloidin (red) marking the cortical actin within cells, and green marking the electroporated cells. Scale bar: 100 µm.

(E) The merged image of a section of the Cdh-2 LOF (pCAG-DN-Cdh-2) electroporated dorsal forebrain region at HH19, with DAPI (blue) marking the nuclei of neuroepithelial cells, phalloidin (red) marking the cortical actin within cells, and green marking the electroporated cells. Scale bar: 100 µm.

(F) The merged image of a section of the GOF of Cdh-2 (pCAG-Cdh-2-FL) electroporated dorsal forebrain region at HH19, with DAPI (blue) marking the nuclei of neuroepithelial cells, phalloidin (red) marking the cortical actin within cells, and green marking the electroporated cells. Scale bar: 100 µm.

(G, H, I) Phalloidin intensity profile of the neuroepithelium from the apical and basal surfaces from forebrains electroporated with constructs for control, LOF, and GOF of Cdh-2, at the midline apex (G), midline vortex (H), and dorsal lateral regions (I), at HH23. The fluorescence intensity of phalloidin was measured up to 80 microns into the cells from both the apical and basal surfaces. Intensity was normalized to a range of 0 to 1 by dividing it by the highest intensity, which was 85 for the control and all test groups. Control is shown in red, Cdh-2 LOF in cyan, and Cdh-2 GOF in green in all the plots. For every N, 30 lines of 80 AU were drawn, and mean value was calculated for each N.

(J, K) Phalloidin intensity profile of the neuroepithelium from the apical and basal surfaces from forebrains electroporated with constructs for control, LOF, and GOF of Cdh-2, at the midline (J) and dorsal lateral regions (K), at HH19. The fluorescence intensity of phalloidin was measured up to 80 microns into the cells from both the apical and basal surfaces. Intensity was normalized to a range of 0 to 1 by dividing it by the highest intensity, which was 85 for the control and all test groups. Control is shown in red, Cdh-2 LOF in cyan, and Cdh-2 GOF in green in all the plots. For every N, 30 lines of 80 AU were drawn, and mean value was calculated for each N.

(L) A schematic of the neuroepithelial cells from the dorsal forebrain region, showing Cdh-2 distribution (red circles) and cortical F-actin levels (yellow dashed lines) in the unmanipulated control forebrain at HH18 (prior to onset of morphogenesis) and at HH23 (W-shaped invagination formed). Further changes in Cdh-2 distribution (red circles) and cortical F-actin levels (yellow dashed lines) are shown when Cdh-2 is perturbed through LOF and GOF manipulations.

Supplementary Materials

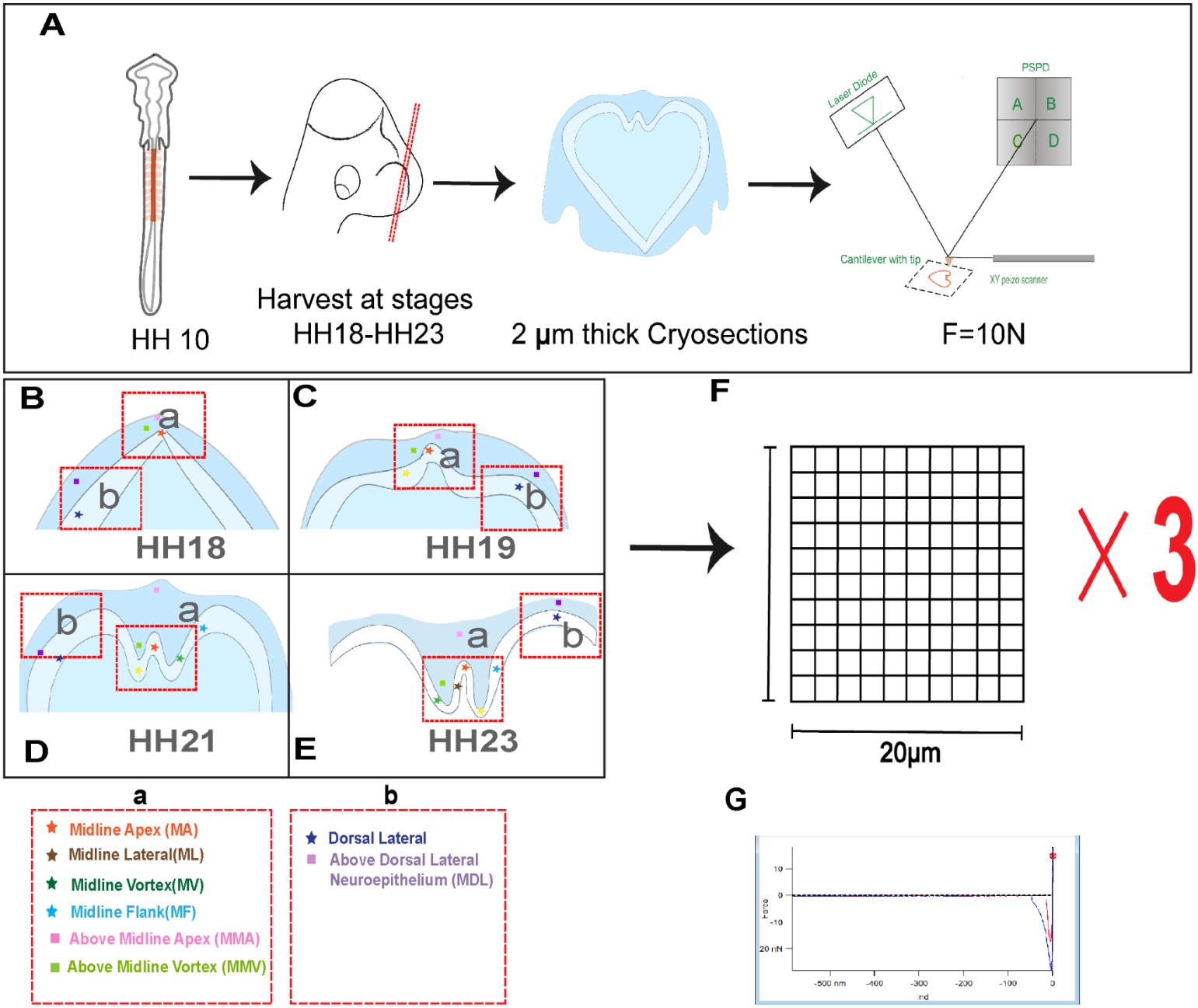

Fig. S1. An optimized protocol for force mapping in the chick forebrain.

(A) A schematic for the optimised protocol developed for measuring stiffness of the chick forebrain using atomic force microscopy (AFM) and an illustration of contact mode AFM whereby a finely pointed tip mounted on a cantilever is used to perform detailed scans of samples and a laser beam is used to sense the bending of the cantilever as its tip hits the surface. The Young's modulus values obtained are used to determine the stiffness of the material. For the dorsal

forebrain tissues a precise force of 10 nN was applied to the cantilever and its resulting deflection was measured to determine the stiffness.

(B, C, D, E) Schematic of coronal sections of the dorsal forebrain at sstages HH18, HH19, HH21 and HH23 with red-dashed outline boxes denoting the regions of the midline (a) and dorsolateral (b) tissues where AFM was used to measure stiffness. The various subdomains named MA, ML, MV, MF and DL within the neuroepithelium are marked with coloured stars. The various subdomains of the mesenchyme named MMV, MMA and MDL are marked by coloured squares.

(F) Schematic depicting the 20 X 20 μm^2 area within each subdomain which was further divided into 100 squares, and the 100 squares in three such 20 X 20 μm^2 were scanned to measure Young's modulus for each N.

(G) A representative Force vs Indentation Curve obtained after scanning with the AFM probe in each of the 100 squares shown in (F). 100 such graphs are combined to produce the heat map of one 20 X 20 μm^2 shown in Fig. S2.

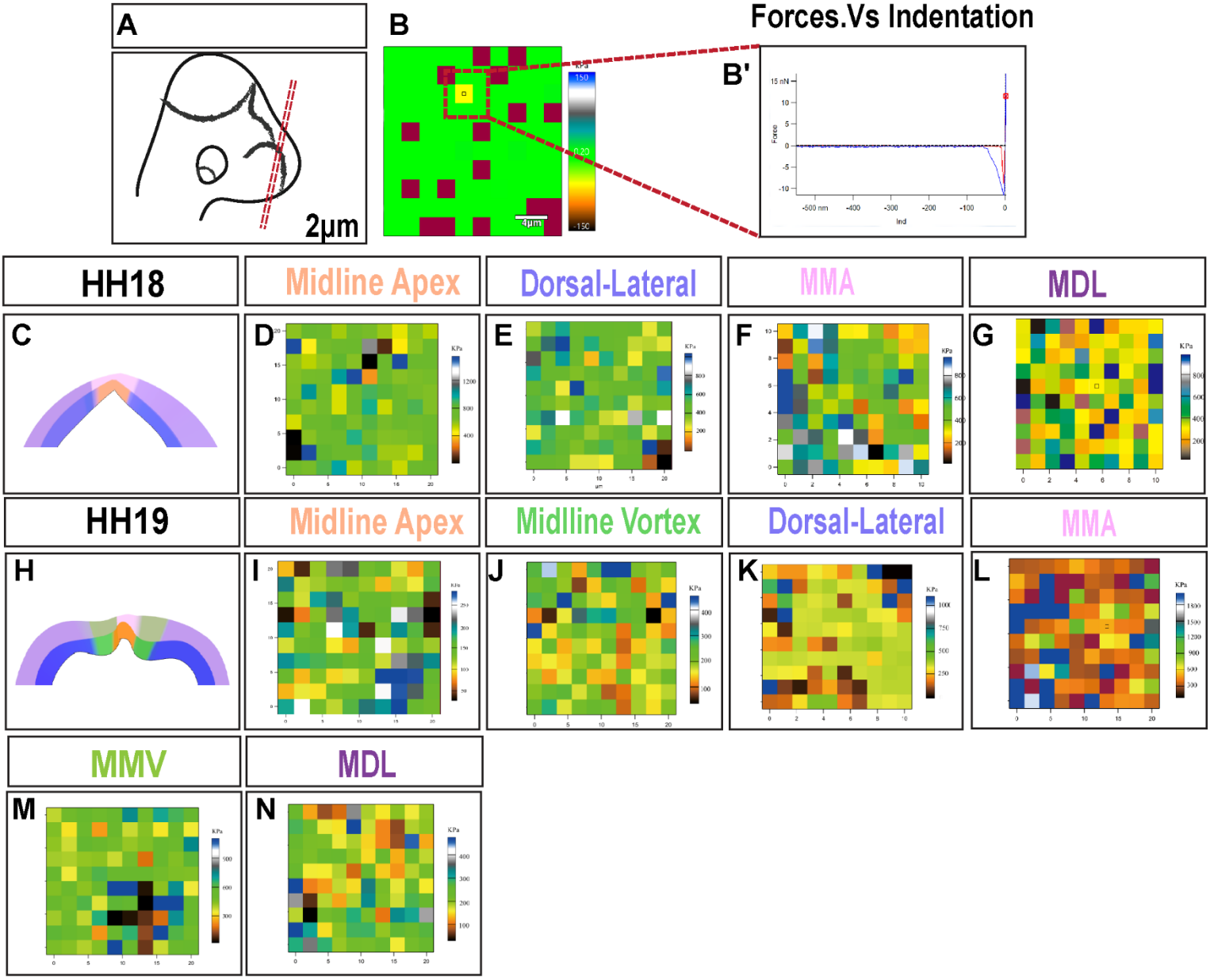

Fig. S2. Heat maps for the measured Young's modulus in the chick forebrain at HH18 and HH19.

(A) A schematic representation of the chick forebrain with the red dashed line demarcating plane in the middle posterior region from which 2 µm thick coronal slices were taken.

(B) Representative heat map of Young's Modulus (YM) measured for each of 100 squares within a 20*20 µm² area of each subdomain of the dorsal forebrain tissues (neuroepithelium and mesenchyme) that were scanned to measure YM in triplicate.

(B') Representative Force vs Indentation Curve for one representative square (in the red dashed box) out of the 100 square heat maps of 20*20 µm² area shown B.

(C) A schematic representation of a coronal slice from the middle posterior region of the chick dorsal forebrain at HH18 with distinct colours marking subdomains of the roof plate neuroepithelium and overlying mesenchyme.

(D, E and F, G) The representative heat maps for the subdomains of the neuroepithelium (midline apex and dorsal lateral) and the mesenchyme (MMA and MDL) at HH18. For each region, a 20*20 μm^2 area was scanned to measure YM in triplicate.

(H) A schematic representation of a coronal slice from the middle posterior region of the chick dorsal forebrain at HH19 with distinct colours marking subdomains of the roof plate neuroepithelium and overlying mesenchyme.

(I, J, K and L, M, N) The representative heat maps for the subdomains of the neuroepithelium (Midline Apex, Midline Vortex and Dorsal-Lateral) and the mesenchyme (MMA, MMV and MDL) at HH19. For each region, a 20*20 μm^2 area was scanned to measure YM in triplicate.

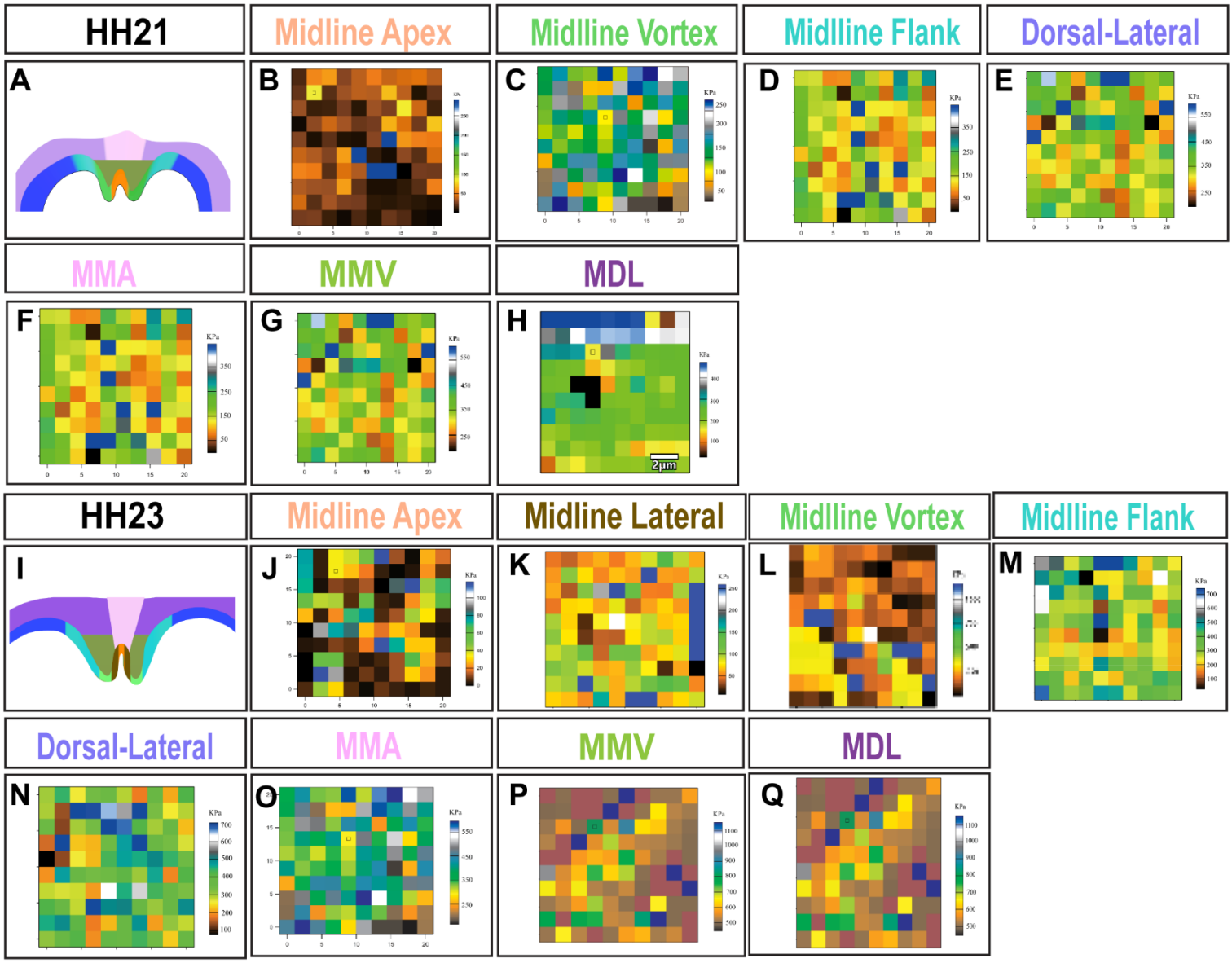

Fig. S3. Heat maps for the measured Young's modulus in the chick forebrain at HH21 and HH23.

(A) A schematic representation of a coronal slice from the middle posterior region of the chick dorsal forebrain at HH21 with distinct colours marking subdomains of the roof plate neuroepithelium and overlying mesenchyme.

(B, C, D, E) The representative heat maps for the subdomains of the neuroepithelium (Midline Apex, Midline Vortex, Midline Flank and Dorsal-Lateral) at HH21. For each region, a 20*20 µm² area was scanned to measure YM in triplicate.

(F, G, H) The representative heat maps for the subdomains of the mesenchyme (MMA, MMV and MDL) at HH21. For each region, a 20*20 µm² area was scanned to measure YM in triplicate.

(I) A schematic representation of a coronal slice from the middle posterior region of the chick dorsal forebrain at HH23 with distinct colours marking subdomains of the roof plate neuroepithelium and overlying mesenchyme.

(J, K, L, M, N) The representative heat maps for the subdomains of the neuroepithelium (Midline Apex, Midline Lateral, Midline Vortex, Midline Flank and Dorsal-Lateral) at HH21. For each region, a 20*20 μm^2 area was scanned to measure YM in triplicate.

(O, P, Q) The representative heat maps for the subdomains of the mesenchyme (MMA, MMV and MDL) at HH23. For each region, a 20*20 μm^2 area was scanned to measure YM in triplicate.

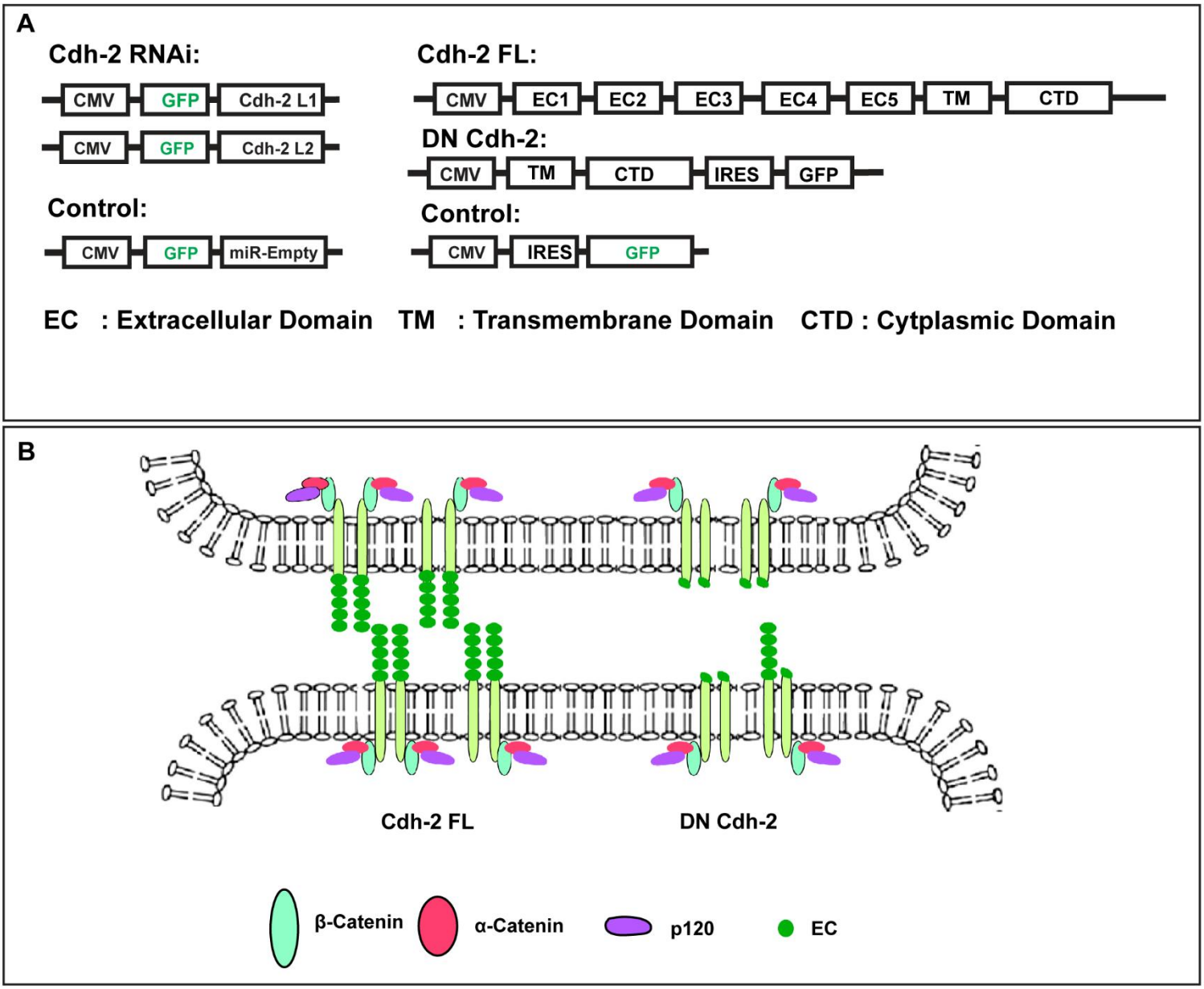

Fig. S4. Design and schematic of Cdh-2 gain- and loss-of-function constructs.

(A) Schematic of constructs used for loss of function and gain of function of Cdh-2.

(B) Strategy for creating loss of function of Cdh-2 through overexpression of dominant negative Cdh-2 (DN-Cdh-2). The schematic shows Cdh-2 with intact extracellular and intracellular domains, alongside a version of Cdh-2 that lacks the extracellular domain, resulting in a dominant negative variant (DN-Cdh-2) created by removing 5 tandem repeats from the extracellular domain.

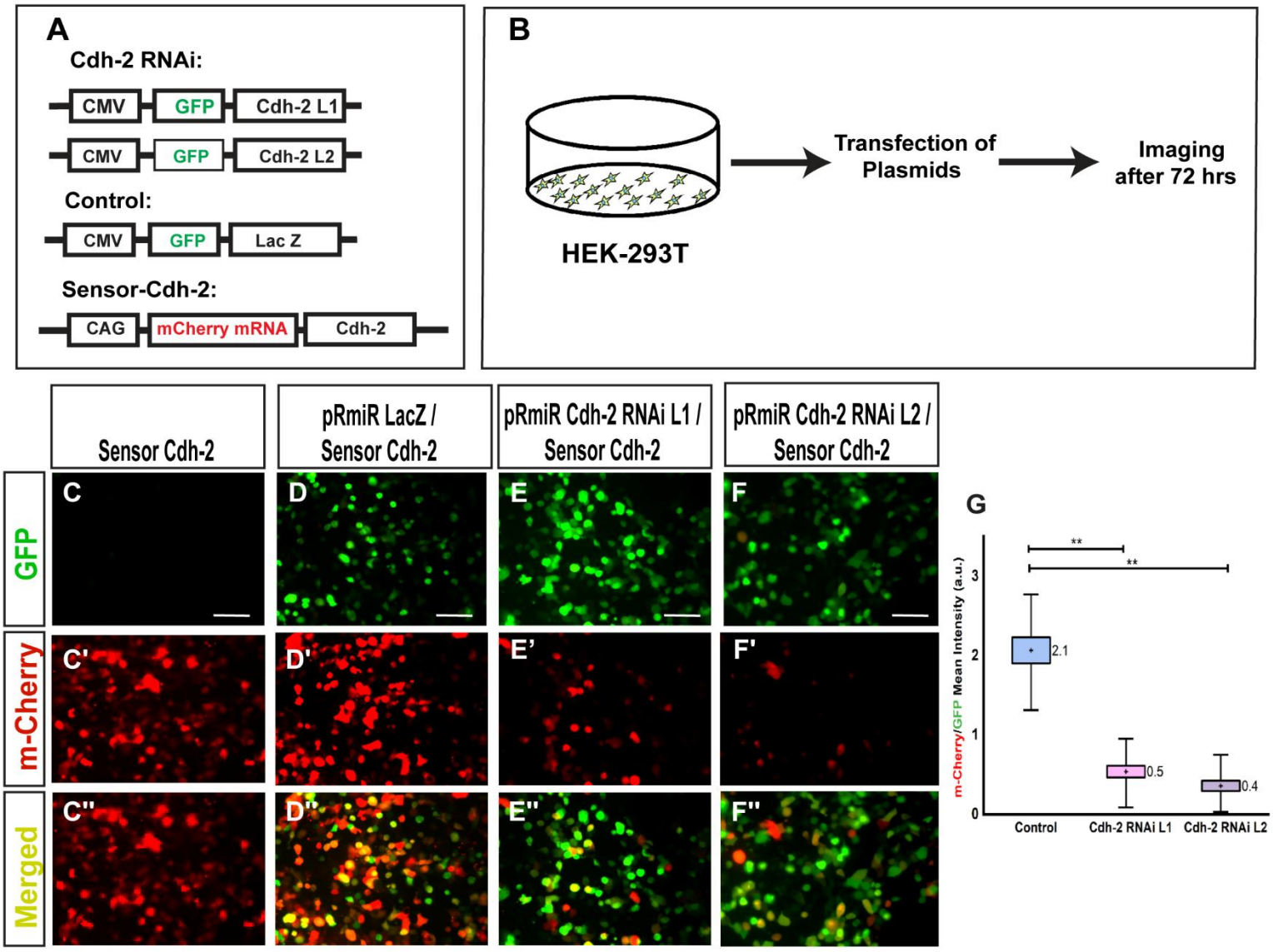

Fig. S5. Sensor assay to determine the efficacy of Cdh-2 RNAi constructs.

(A) Schematic representation of the constructs used to test the efficacy of RNAi oligos designed for knocking down Cdh-2 expression in HEK293T cells using the sensor assay.

(B) Schematic of the experimental design for the sensor assay.

(C, C' and C") HEK293T cells transfected with Sensor-Cdh-2 expressing mCherry alone. (C) GFP fluorescence (green), (C′) mCherry fluorescence (red) and (C″) Merged image for the HEK293T cells transfected with Sensor-Cdh-2 alone. Scale bar: 100µm

(D, D' and D") HEK293T cells co-transfected with Sensor-Cdh-2 and control RNAi-LacZ expressing GFP. (D) GFP fluorescence (green), (D′) mCherry fluorescence (red) and (D″) Merged images for the HEK293T cells co-transfected with Sensor-Cdh-2 and PRmiR-LacZ. Scale bar: 100µm

(E, E’ and E’’) HEK293T cells co-transfected with Sensor-Cdh-2 and PRmiR-Cdh-2 L1. (E) GFP fluorescence (green), (E′) mCherry fluorescence (red) and (E″) Merged images for the HEK293T cells transfected with Sensor-Cdh- 2 and PRmiR-Cdh-2 L1. Scale bar: 100µm

(F, F’ and F’’) HEK293T cells co-transfected with Sensor-Cdh-2 and PRmiR-Cdh-2 L2 expressing GFP. (F) GFP fluorescence (green), (F′) mCherry fluorescence (red) and (F″) Merged images for the HEK293T cells transfected with Sensor-Cdh-2 and PRmiR- Cdh-2-L2. Scale bar: 100µm

(G) Quantification of mean mCherry/GFP intensity for HEK293T cells transfected with only Sensor-Cdh-2, Sensor-Cdh-2 + PRmiR-Cdh-2 L1 and Sensor-Cdh-2 + PRmiR-Cdh-2-L2. Unpaired t-test using OriginPro software for determination of statistical significance. $p<0.01$ for all the comparisons. Error bars indicate mean±SEM. Scale bar: 100 µm for all experiments. Green fluorescence indicates cells where the RNAi construct effectively knocked down the sensor and yellow fluorescence indicates cells that have sensor expression (m-cherry) in the presence of RNAi (GFP) indicating a failure of knockdown. N=3 for all experiments.

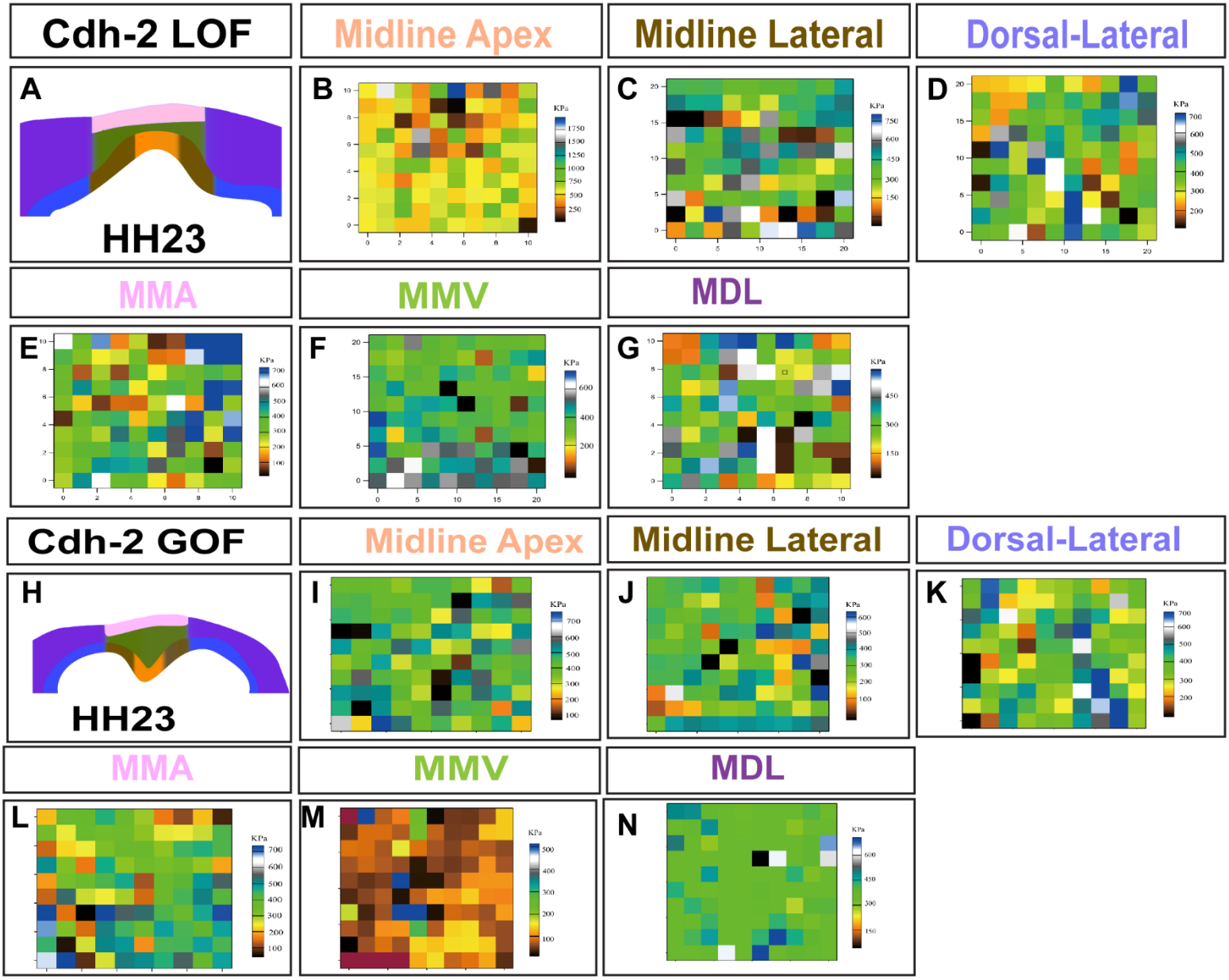

Fig. S6. Heat maps for measured Young's modulus in the chick forebrain at HH23 following modulation of Cdh-2.

(A) A schematic representation of a coronal slice from the middle posterior region of the chick dorsal forebrain upon LOF of Cdh-2 at HH23 with distinct colours marking subdomains of the roof plate neuroepithelium and overlying mesenchyme.

(B, C, D) The representative heat maps for the subdomains of the neuroepithelium (Midline Apex, Midline Lateral and Dorsal-Lateral) upon LOF of Cdh-2 at HH23. For each region, a 20*20 μm² area was scanned to measure YM in triplicate.

(E, F, G) The representative heat maps for the subdomains of the mesenchyme (MMA, MMV and MDL) upon LOF of Cdh-2 at HH23. For each region, a 20*20 μm^2 area was scanned to measure YM in triplicate.

(H) A schematic representation of a coronal slice from the middle posterior region of the chick dorsal forebrain upon GOF of Cdh-2 at HH23 with distinct colours marking subdomains of the roof plate neuroepithelium and overlying mesenchyme.

(I, J, K) The representative heat maps for the subdomains of the neuroepithelium (Midline Apex, Midline Lateral and Dorsal-Lateral) upon GOF of Cdh-2 at HH23. For each region, a 20*20 μm^2 area was scanned to measure YM in triplicate.

(L, M, N) The representative heat maps for the subdomains of the mesenchyme (MMA, MMV and MDL) upon GOF of Cdh-2 at HH23. For each region, a 20*20 μm^2 area was scanned to measure YM in triplicate.

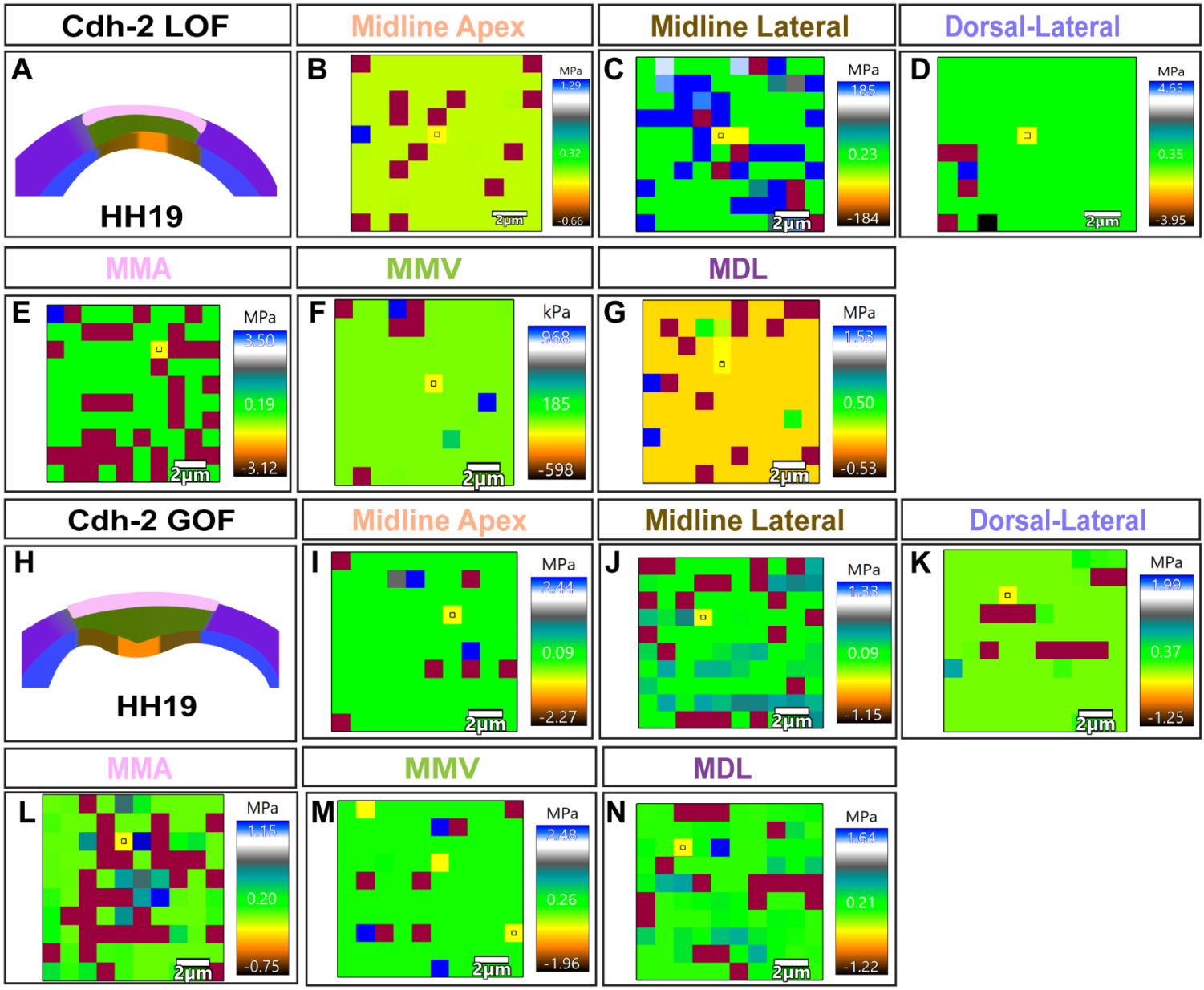

Fig. S7. Heat maps for measured Young's modulus in the chick forebrain at HH19 following modulation of Cdh-2.

(A) A schematic representation of a coronal slice from the middle posterior region of the chick dorsal forebrain upon LOF of Cdh-2 at HH19 with distinct colours marking subdomains of the roof plate neuroepithelium and overlying mesenchyme.

(B, C, D) The representative heat maps for the subdomains of the neuroepithelium (Midline Apex, Midline Lateral and Dorsal-Lateral) upon LOF of Cdh-2 at HH19. For each region, a 20*20 µm² area was scanned to measure YM in triplicate.

(E,F,G) The representative heat maps for the subdomains of the mesenchyme (MMA, MMV and MDL) upon LOF of Cdh-2 at HH19. For each region, a 20*20 μm^2 area was scanned to measure YM in triplicate.

(H) A schematic representation of a coronal slice from the middle posterior region of the chick dorsal forebrain upon GOF of Cdh-2 at HH19 with distinct colours marking subdomains of the roof plate neuroepithelium and overlying mesenchyme.

(I,J,K) The representative heat maps for the subdomains of the neuroepithelium (Midline Apex, Midline Lateral and Dorsal-Lateral) upon GOF of Cdh-2 at HH19. For each region, a 20*20 μm^2 area was scanned to measure YM in triplicate.

(L,M,N) The representative heat maps for the subdomains of the mesenchyme (MMA, MMV and MDL) upon GOF of Cdh-2 at HH19. For each region, a 20*20 μm^2 area was scanned to measure YM in triplicate.

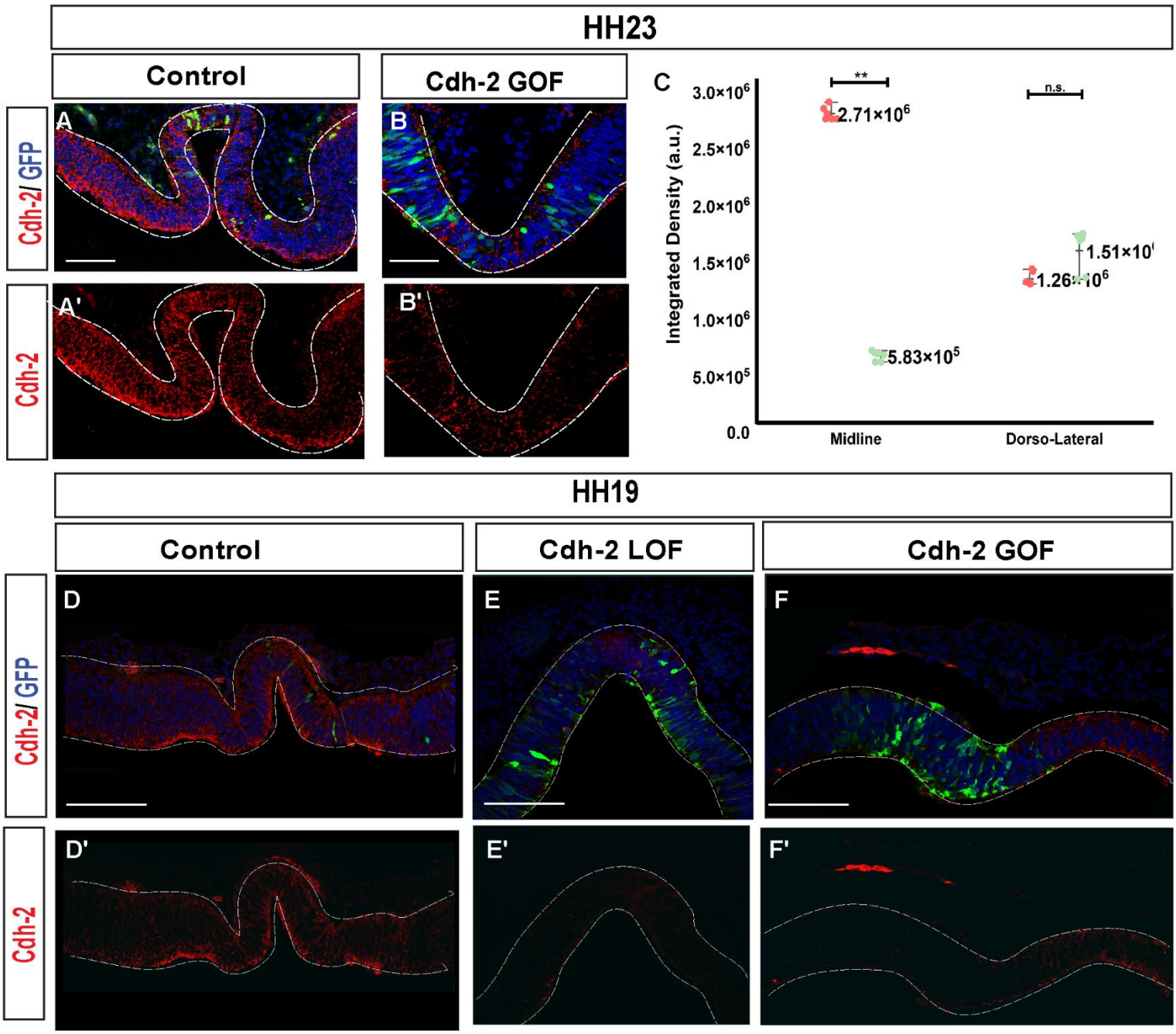

Fig. S8. Impact of Cdh-2 manipulation on the levels of endogenous Cdh-2.

Integration density of Cdh-2 was measured to quantify the amount of Cdh-2 protein and determine the effect of Cdh-2 overexpression (Cdh-2 GOF) in midline and dorsal lateral regions of neuroepithelium**.**

(A) Merged image of a section of chick forebrain electroporated with the control construct pCAG-GFP at HH23; DAPI (blue) marks nuclei, the green fluorescent signal demarcates the domain of electroporation, and red fluorescence indicates immunostaining of Cdh-2 protein. (A') Image of the same section as in (A) with red signal indicating Cdh-2 immunostaining. Scale bar: 100µm.

(B) The merged image shows a section of the chick forebrain co-electroporated with pCAG-GFP and Cdh-2 FL at HH23; DAPI (blue) marks the nuclei, the green fluorescent signal indicates the domain of electroporation, and the red fluorescence indicates immunostaining of Cdh-2 protein. (B') Image of the same section as in (B) with red signal indicating Cdh-2 immunostaining. Scale bar: 100µm.

3*3 boxes were marked in the midline and dorsal lateral regions in which the integrated density of Cdh-2 (red) was calculated.

(C) Dot plot comparing the integrated density of Cdh-2 (red) in the midline and dorsal lateral regions between the test and control groups. Error bars indicate mean±SEM, $p \leq 0.01$. N=6.

(D) Merged image of a section of chick forebrain electroporated with the control construct (pCAG-GFP) at HH19; DAPI (blue) marks nuclei, the green fluorescent signal demarcates the domain of electroporation, and red marks Cdh-2 immunostaining. (D') Image of the same section as in (D) with red signal indicating Cdh-2 immunostaining. Scale bar: 100µm.

(E) Merged image of a section of the chick forebrain electroporated with DN-Cdh-2 (LOF for Cdh-2) at HH19; DAPI (blue) marks nuclei, the green fluorescent signal demarcates the extent of electroporation, and red marks Cdh-2 immunostaining. (E') Image of the same section as in (E) with red signal denoting Cdh-2 immunostaining. Scale bar: 100µm.

(F) Merged image of a section of the chick forebrain co-electroporated with pCAG-GFP and Cdh-2 FL (GOF for Cdh-2) at HH19; DAPI (blue) marks nuclei, the green fluorescent signal demarcates the extent of electroporation, and red marks Cdh-2 immunostaining. (F') Image of the same section as in (F) with red signal denoting Cdh-2 immunostaining. Scale bar: 100µm.

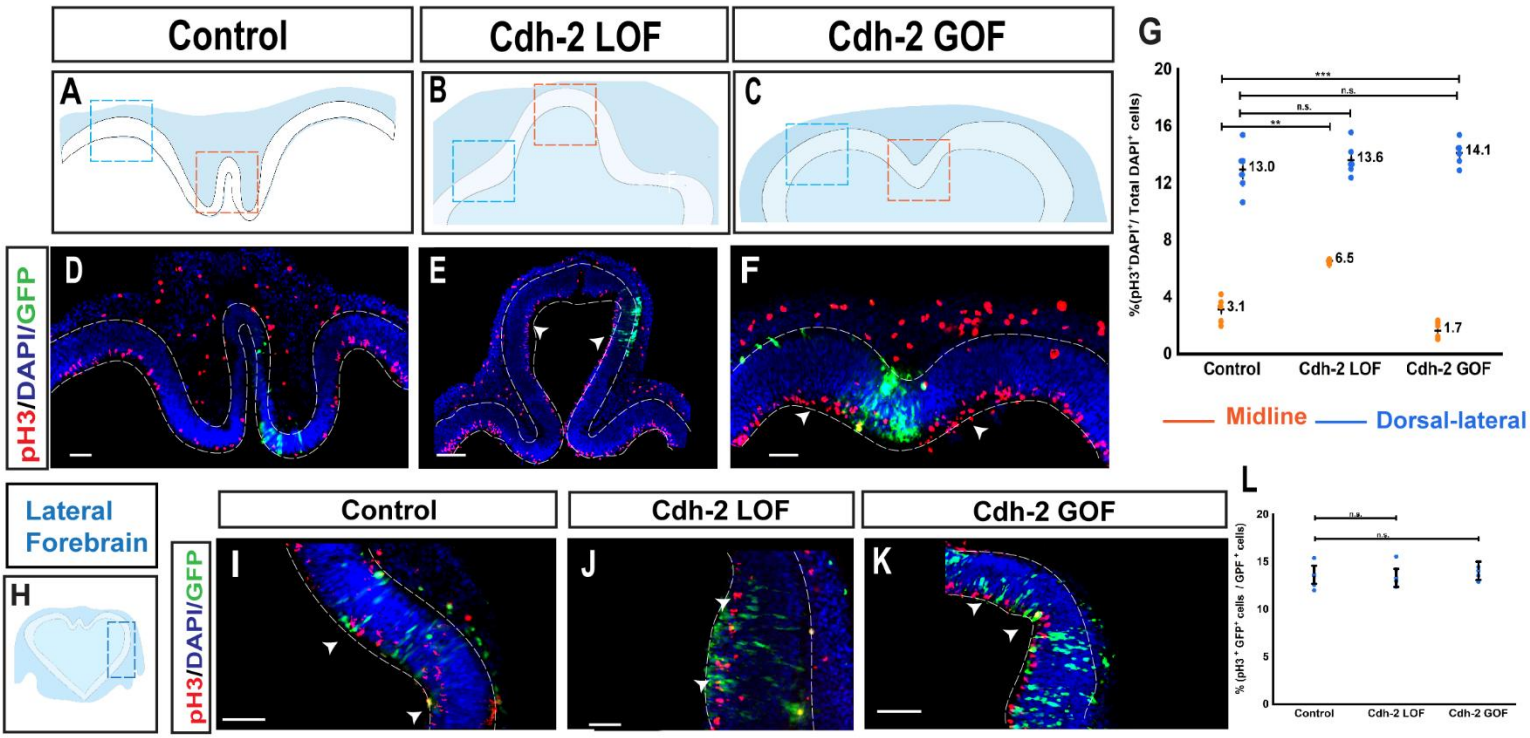

Fig. S9. Effect of Cdh-2 modulation on the cell proliferation.

(A, B, C) This schematic illustration depicts the region of the medial (orange boxed region) and dorsolateral (blue boxed region) neuroepithelium where PH3-positive cells were quantified to determine the effect of Cdh-2 perturbation on cell proliferation.

(D, E, F) A merged image shows a section of the chick forebrain roof plate that was electroporated with (D) control construct pCAG-GFP, E) DN-Cdh-2 construct and (F) Cdh-2 FL and pCAG-GFP. The nuclei of neuroepithelial cells are identified by DAPI staining (blue), and the domain of electroporation is indicated by green fluorescence. Red fluorescence indicates PH3-positive proliferating cells. Scale bar: 100µm.

(G) Quantification of percentage of DAPI-positive cells that are PH3 positive, statistical significance determined using an unpaired t-test, Origin 2024b. (N=5), $p \leq 0.001$.

(H) Schematic of the section of the chick forebrain at HH23 with the blue dashed box indicating the position of the lateral region of the neuroepithelium used to quantify PH3 and DAPI.

(I, J, K) Merged image of a section of the chick forebrain roof plate electroporated with (I) the control construct IRES-GFP, (J) the DN-Cdh-2 construct and (K) the Cdh-2 FL and pCAG-GFP constructs where DAPI staining (blue) marks the nuclei of neuroepithelial cells, green fluorescence demarcates the domain of electroporation and Red fluorescence marks the PH3-positive proliferating cells. Scale bar: 100µm.

(L) Box plot showing quantification of the percentage of double positive (PH3+ and GFP+) cells by total GFP+ positive cells, unpaired t-test using Origin 2024b software was carried out for statistical significance. (N=4), $p \leq 0.001$.

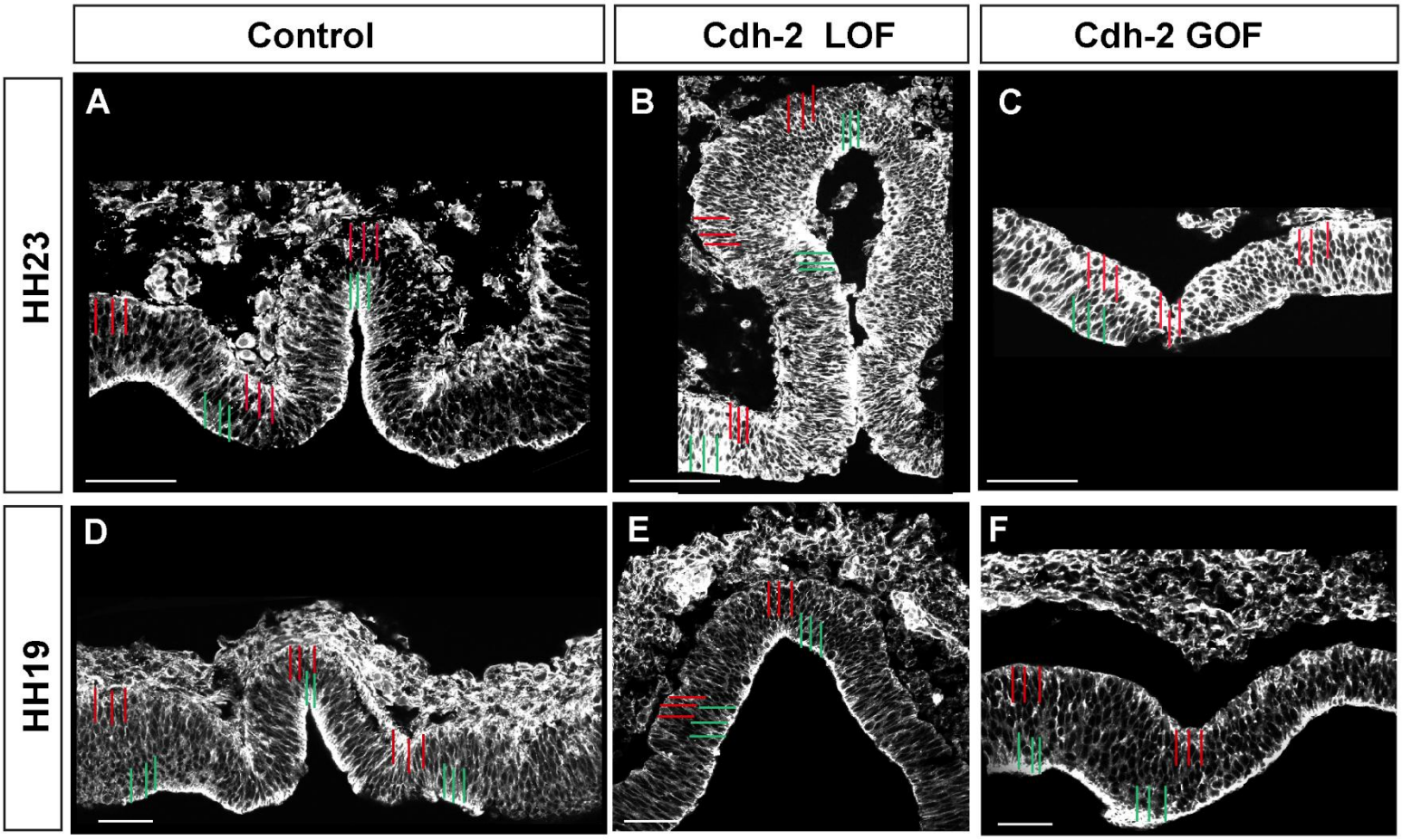

Fig. S10. Effect of Cdh-2 modulation on cortical F-actin distribution in neuroepithelial cells.

(A, B, C) Fluorescence intensity of phalloidin was measured up to 80 a.u into the cells from both the apical and basal surfaces (orange and green lines) for sections of the forebrain roof plate at HH23 electroporated with (A) the control construct, (B) the LOF for Cdh-2 construct and (C) the GOF for Cdh-2 construct at HH23. The green lines mark the neuroepithelium on the apical surface, while the orange lines mark the neuroepithelium on the basal surface. The intensity was measured at the midline apex (MA), midline vortex (MV), and dorsal lateral (DL) regions of the neuroepithelium. Scale bar: 100µm.

(D, E, F) Fluorescence intensity of phalloidin was measured up to 80 a.u into the cells from both the apical and basal surfaces (orange and green lines) for sections of the forebrain roof plate at HH19 electroporated with (D) the control construct, (E) the LOF for Cdh-2 construct and (F) the GOF for Cdh-2 construct at HH23. The green lines mark the neuroepithelium on the apical surface, while the orange lines mark the neuroepithelium on the basal surface. The intensity was measured at the midline apex (MA), midline vortex (MV), and dorsal lateral (DL) regions of the neuroepithelium. Scale bar: 100µm.